



SPLUS J142445.34–254247.1: An *r*-process–enhanced, Actinide-boost, Extremely Metal-poor Star Observed with GHOST

Vinicio M. Placco¹ , Felipe Almeida-Fernandes² , Erika M. Holmbeck^{3,22} , Ian U. Roederer^{4,5,6} , Mohammad K. Mardini^{7,8,9} , Christian R. Hayes¹⁰ , Kim Venn¹¹ , Kristin Chiboucas¹² , Emily Deibert¹³ , Roberto Gamen¹⁴ , Jeong-Eun Heo¹³ , Miji Jeong¹⁵ , Venu Kalari¹³ , Eder Martioli¹⁶ , Siyi Xu¹² , Ruben Diaz¹³ , Manuel Gomez-Jimenez¹³, David Henderson¹², Pablo Prado¹³, Carlos Quiroz¹³ , Roque Ruiz-Carmona¹³ , Chris Simpson¹² , Cristian Urrutia¹³, Alan W. McConnachie¹⁰ , John Pazder^{10,11}, Gregory Burley¹⁰, Michael Ireland¹⁷ , Fletcher Waller¹¹, Trystyn A. M. Berg^{10,18} , J. Gordon Robertson^{19,20} , Zachary Hartman¹² , David O. Jones^{12,21} , Kathleen Labrie¹² , Gabriel Perez¹³ , Susan Ridgway¹, and Joanna Thomas-Osip¹³

¹ NSF's NOIRLab, Tucson, AZ 85719, USA; vinicio.placco@noirlab.edu

² Departamento de Astronomia, Instituto de Astronomia, Geofísica e Ciências Atmosféricas da USP, Cidade Universitária, 05508-900 São Paulo, SP, Brazil

³ Observatories of the Carnegie Institution for Science, Pasadena, CA 91101, USA

⁴ Department of Physics, North Carolina State University, Raleigh, NC 27695, USA

⁵ Department of Astronomy, University of Michigan, Ann Arbor, MI 48109, USA

⁶ Joint Institute for Nuclear Astrophysics—Center for the Evolution of the Elements (JINA-CEE), USA

⁷ Department of Physics, Zarqa University, Zarqa 13110, Jordan

⁸ Kavli IPMU (WPI), UTIAS, The University of Tokyo, Kashiwa, Chiba 277-8583, Japan

⁹ Institute for AI and Beyond, The University of Tokyo 7-3-1 Hongo, Bunkyo-ku, Tokyo 113-8655, Japan

¹⁰ NRC Herzberg Astronomy and Astrophysics Research Centre, 5071 West Saanich Road, Victoria, BC V9E 2E7, Canada

¹¹ Department of Physics and Astronomy, University of Victoria, Victoria, BC V8W 3P2, Canada

¹² Gemini Observatory/NSF's NOIRLab, 670 N. A'ohoku Place, Hilo, HI 96720, USA

¹³ Gemini Observatory/NSF's NOIRLab, Casilla 603, La Serena, Chile

¹⁴ Instituto de Astrofísica de La Plata, CONICET-UNLP, Paseo del Bosque s/n, 1900 La Plata, Argentina

¹⁵ Department of Astronomy, Space Science, and Geology, Chungnam National University, Daejeon 34134, Republic of Korea

¹⁶ Laboratório Nacional de Astrofísica, Rua Estados Unidos 154, 37504-364 Itajubá, MG, Brazil

¹⁷ Research School of Astronomy and Astrophysics, Australian National University, Canberra 2611, Australia

¹⁸ Dipartimento di Fisica G. Occhialini, Università degli Studi di Milano Bicocca, Piazza della Scienza 3, I-20126 Milano, Italy

¹⁹ Australian Astronomical Optics, Macquarie University, 105 Delhi Road, North Ryde, NSW 2113, Australia

²⁰ School of Physics, University of Sydney, NSW 2006, Australia

²¹ Institute for Astronomy, University of Hawaii, 640 N. A'ohoku Place, Hilo, HI 96720, USA

Received 2023 September 22; revised 2023 October 24; accepted 2023 October 25; published 2023 December 6

Abstract

We report on a chemo-dynamical analysis of SPLUS J142445.34–254247.1 (SPLUS J1424–2542), an extremely metal-poor halo star enhanced in elements formed by the rapid neutron-capture process (*r*-process). This star was first selected as a metal-poor candidate from its narrowband S-PLUS photometry and followed up spectroscopically in medium resolution with Gemini-South/GMOS, which confirmed its low-metallicity status. High-resolution spectroscopy was gathered with GHOST at Gemini-South, allowing for the determination of the chemical abundances for 36 elements, from carbon to thorium. At [Fe/H] = −3.39, SPLUS J1424–2542 is one of the lowest-metallicity stars with measured Th and has the highest log ϵ (Th/Eu) observed to date, making it part of the “actinide-boost” category of *r*-process–enhanced stars. The analysis presented here suggests that the gas cloud from which SPLUS J1424–2542 formed must have been enriched by at least two progenitor populations. The light-element ($Z \leq 30$) abundance pattern is consistent with the yields from a supernova explosion of metal-free stars with 11.3–13.4 M_{\odot} , and the heavy-element ($Z \geq 38$) abundance pattern can be reproduced by the yields from a neutron star merger (1.66 M_{\odot} and 1.27 M_{\odot}) event. A kinematical analysis also reveals that SPLUS J1424–2542 is a low-mass, old halo star with a likely in situ origin, not associated with any known early merger events in the Milky Way.

Unified Astronomy Thesaurus concepts: High resolution spectroscopy (2096); Stellar atmospheres (1584); Narrow band photometry (1088); Chemical abundances (224); Metallicity (1031)

Supporting material: machine-readable table

1. Introduction

The element europium (Eu; $Z = 63$), formed mainly by the rapid neutron-capture process (*r*-process; Burbidge et al. 1957),

was identified in the spectrum of the Sun by Dyson (1906) from observations taken during the 1900, 1901, and 1905 total solar eclipses. In other stars, some of the first measurements of Eu also date back to the early 1900s (Lunt 1907; Baxandall 1913). In fact, Lunt (1907) describes Eu as a “disturbing element” when trying to determine the radial velocities for the α -Boötis and β -Geminorum stars from a calcium absorption feature.²³ Since then, Eu has

²² NHFP Hubble Fellow.

Original content from this work may be used under the terms of the Creative Commons Attribution 4.0 licence. Any further distribution of this work must maintain attribution to the author(s) and the title of the work, journal citation and DOI.

²³ For the purpose of the present work, this calcium line is the actual “disturbing element” when performing the spectral synthesis of the Eu $\lambda 4435$ line, which is shown in later sections.

established itself as a crucial tracer of the operation of the *r*-process in the Galaxy and beyond, with a large number of measurable absorption features in the optical wavelength regime.

In this context, low-mass, long-lived, old stars in the Galactic halo hold in their atmospheres valuable insights into the nucleosynthesis in the early Universe and the formation of heavy elements. They are the key to understanding the chemical evolution of the Universe. From a theoretical perspective, the nucleosynthetic pathways from hydrogen to the heavy elements (loosely defined as $Z > 30$) have been understood for almost 80 yr (e.g., Hoyle 1946). These heavy elements were identified in stellar atmospheres even before (Merrill 1926; and references in the paragraph above), but it was only in the past 50 yr or so that high-resolution spectroscopy was able to quantify the chemical abundances in a statistically relevant and consistent way (Cowley et al. 1973; Spite & Spite 1978; Luck & Bond 1981; Truran 1981; Sneden & Pilachowski 1985; Gilroy et al. 1988; Sneden et al. 1994; to name a few). The past 25 yr have seen a tremendous increase in the number of high-resolution spectroscopic observations of metal-poor stars ($[\text{Fe}/\text{H}] \lesssim -1.0$)²⁴ with enhancement in elements formed by the *r*-process, in particular the so-called *r*-II stars ($[\text{Eu}/\text{Fe}] > +1$ and $[\text{Ba}/\text{Eu}] < 0$; Frebel 2018).²⁵

The nucleosynthesis of *r*-process elements requires high neutron fluxes and it is believed to occur in extreme astrophysical events, such as the aftermath of neutron star mergers (Goriely et al. 2011; Abbott et al. 2017; Drout et al. 2017; Shappee et al. 2017) or the evolution of massive stars (Grichener & Soker 2019; Siegel et al. 2019), and the subsequent pollution of the interstellar medium by these elements has allowed the formation of such peculiar low-mass *r*-II stars. Understanding the properties and distribution of such stars is crucial for constraining *r*-process models and gaining insights into the conditions prevalent in the early Universe. Recent studies have also provided insight into the astrophysical environments that would harbor such extreme events and enable the formation of *r*-II stars. As an example, dwarf galaxies and stellar overdensities were found to contain low-metallicity, *r*-process-enhanced stars (Vincenzo et al. 2015; Ji et al. 2016; Hansen et al. 2017; Roederer et al. 2018a; Yuan et al. 2020; Gudin et al. 2021; Abuchaim et al. 2023; Shank et al. 2023).

r-II stars are not a common occurrence within very metal-poor samples in the Milky Way. The first systematic search for such objects was the Hamburg/ESO *R*-process Enhanced star Survey (HERES; Christlieb et al. 2004b; Barklem et al. 2005), which obtained data for 253 metal-poor halo stars. More recently, the *R*-Process Alliance (RPA; Sakari et al. 2018a; Hansen et al. 2018; Ezzeddine et al. 2020; Holmbeck et al. 2020) has been making outstanding progress in further discovering and analyzing *r*-process enhanced stars. Both HERES and RPA adopt a two-step approach, first identifying metal-poor stars from medium-resolution ($R \sim 2000$) spectroscopy (Frebel et al. 2006; Placco et al. 2018, 2019) then collecting “snapshot” (signal-to-noise ratio, $\text{S/N} \sim 50$ and $R \sim 20,000$) spectra for the confirmed candidates. Further

²⁴ $[\text{A}/\text{B}] = \log(N_{\text{A}}/N_{\text{B}})_{\star} - \log(N_{\text{A}}/N_{\text{B}})_{\odot}$, where N is the number density of atoms of a given element in the star (\star) and the Sun (\odot), respectively.

²⁵ More recently, Holmbeck et al. (2020) has empirically redefined the *r*-II classification boundary to be $[\text{Eu}/\text{Fe}] > +0.7$.

studies are then conducted for the most interesting candidates within those samples (Jonsell et al. 2006; Mashonkina et al. 2010a; Ren et al. 2012; Cui et al. 2013; Mashonkina et al. 2014a; Mashonkina & Christlieb 2014; Hill et al. 2017; Placco et al. 2017; Roederer et al. 2018b; Sakari et al. 2018b; Cain et al. 2018; Gull et al. 2018; Holmbeck et al. 2018; Placco et al. 2020; Roederer et al. 2022; among many others). Even within those somewhat targeted searches, the fraction of *r*-II stars ($[\text{Eu}/\text{Fe}] > +1.0$) found in HERES is 3%, while for RPA is 8%, using data from their four “data release” articles mentioned above. There is a clear need for continuing the identification of such objects in order to constrain properly their occurrence fractions and astrophysical sites.

In this article, we continue in the quest to increase the number of identified *r*-process-enhanced stars in the Milky Way. We present the chemo-dynamical analysis of SPLUS J142445.34–254247.1 (hereafter SPLUS J1424–2542) using data from the recently commissioned Gemini High-resolution Optical SpecTrograph (GHOST) spectrograph at Gemini-South. At $[\text{Fe}/\text{H}] = -3.39$ with a low carbon-to-iron abundance ratio, SPLUS J1424–2542 has a distinctive *r*-process signature with an enhancement in thorium when compared to the scaled solar system *r*-process abundance pattern. From a kinematics perspective, SPLUS J1424–2542 is a low-mass, old halo star with a probable *in situ* origin.

This work is outlined as follows: Section 2 details the target selection and observations, followed by the determination of stellar atmospheric parameters and chemical abundances in Section 3. In Section 4 we analyze the chemical abundance pattern of SPLUS J1424–2542 and its dynamical properties, aiming to infer characteristics of the progenitor population(s). Final remarks and perspectives for future work are presented in Section 5.

2. Target Selection and Observations

In this section, we briefly describe the identification, selection, and spectroscopic follow-up observations of SPLUS J1424–2542. Table 1 lists the basic information and derived quantities of SPLUS J1424–2542, measured in this work and other studies in the literature.²⁶ Further details can also be found in Placco et al. (2022).

2.1. S-PLUS and Gemini/Gemini Multi-Object Spectrograph

SPLUS J1424–2542 was observed as part of the Southern Photometric Local Universe Survey (S-PLUS; Mendes de Oliveira et al. 2019) second data release (DR2; Almeida-Fernandes et al. 2022). S-PLUS has a unique 12 broad- and narrowband filter set, consisting of four Sloan Digital Sky Survey (SDSS; g, r, i, z), one modified SDSS u , and seven narrowband filters. SPLUS J1424–2542 was selected as a metal-poor star candidate by Placco et al. (2022), based on its narrowband metallicity-sensitive colors. These colors, $(\text{J}0395 - \text{J}0410) - (\text{J}0660 - \text{J}0861)$ and $(\text{J}0395 - \text{J}0660) - 2 \times (g - i)$, are listed in Table 1 and place SPLUS J1424–2542 in the same regime as other spectroscopically confirmed low-metallicity stars (see Figures 1 and 7

²⁶ SPLUS J1424–2542 has been independently observed as part of the SkyMapper Southern Survey Data Release 1 (SMSS DR1; Wolf et al. 2018) as SMSS J142445.33–254246.9. It was followed up with medium-resolution spectroscopy ($R \sim 3000$) as part of the search for extremely metal-poor stars conducted by Da Costa et al. (2019). For reference, the atmospheric parameters determined by Da Costa et al. (2019) are provided in Table 1.

Table 1
Properties of SPLUS J1424–2542

Quantity	Symbol	Value	Units	Reference
R.A.	α (J2000)	14:24:45.34	hh:mm:ss.ss	Gaia Collaboration et al. (2023)
Decl.	δ (J2000)	-25:42:47.1	dd:mm:ss.s	Gaia Collaboration et al. (2023)
Galactic longitude	ℓ	327.983	degrees	Gaia Collaboration et al. (2023)
Galactic latitude	b	32.579	degrees	Gaia Collaboration et al. (2023)
Gaia DR3 ID	...	6271613367058424064	...	Gaia Collaboration et al. (2023)
Parallax	ϖ	0.0796 \pm 0.0182	mas	Gaia Collaboration et al. (2023)
Inverse parallax distance	$1/\varpi$	8.13 $^{+1.41}_{-1.05}$	kpc	This study ^a
Distance	d	7.82 $^{+0.95}_{-0.76}$	kpc	Bailer-Jones et al. (2021)
Proper motion (α)	PMRA	-2.643 \pm 0.022	mas yr $^{-1}$	Gaia Collaboration et al. (2023)
Proper motion (δ)	PMDec	0.956 \pm 0.026	mas yr $^{-1}$	Gaia Collaboration et al. (2023)
K magnitude	K	11.538 \pm 0.021	mag	Skrutskie et al. (2006)
G magnitude	G	13.794 \pm 0.003	mag	Gaia Collaboration et al. (2023)
BP magnitude	BP	14.340 \pm 0.003	mag	Gaia Collaboration et al. (2023)
RP magnitude	RP	13.087 \pm 0.004	mag	Gaia Collaboration et al. (2023)
g magnitude	g_{SDSS}	14.435 \pm 0.002	mag	Almeida-Fernandes et al. (2022)
(J0395 – J0410) – (J0660 – J0861)	...	-0.155 \pm 0.011	mag	Placco et al. (2022)
(J0395 – J0660) – 2 \times ($g - i$)	...	-0.315 \pm 0.009	mag	Placco et al. (2022)
Color excess	$E(B - V)$	0.0647 \pm 0.0021	mag	Schlafly & Finkbeiner (2011)
Bolometric correction	BC_V	-0.59 \pm 0.09	mag	Casagrande & Vandenberg (2014)
S/N @3860 Å	S/N	28	pixel $^{-1}$	This study (GHOST)
@4360 Å	...	54	pixel $^{-1}$	This study (GHOST)
@5180 Å	...	139	pixel $^{-1}$	This study (GHOST)
@6540 Å	...	171	pixel $^{-1}$	This study (GHOST)
Effective temperature	T_{eff}	4700 \pm 150	K	Placco et al. (2022) (GMOS)
	...	4750	K	Da Costa et al. (2019)
	...	4762 \pm 36	K	This study (GHOST)
Log of surface gravity	$\log g$	1.48 \pm 0.20	(cgs)	Placco et al. (2022) (GMOS)
	...	1.00	(cgs)	Da Costa et al. (2019)
	...	1.58 \pm 0.11	(cgs)	This study (GHOST)
Microturbulent velocity	ξ	1.60 \pm 0.20	km s $^{-1}$	This study (GHOST)
Metallicity	[Fe/H]	-3.82 \pm 0.20	dex	Placco et al. (2022) (GMOS)
	...	-3.25	dex	Da Costa et al. (2019)
	...	-3.39 \pm 0.12	dex	This study (GHOST)
Age	...	10.09 $^{+2.96}_{-3.12}$	Gyr	Almeida-Fernandes et al. (2023)
Mass	M	0.843 $^{+0.079}_{-0.056}$	M_{\odot}	Almeida-Fernandes et al. (2023)
Radial velocity	RV	-31.2 \pm 0.5	km s $^{-1}$	This study (MJD: 60074.25416667)
Galactocentric coordinates	(X, Y, Z)	(+2.61, -3.50, +4.22)	kpc	This study
Galactic space velocity	(U, V, W)	(-93.0, -29.4, +46.4)	km s $^{-1}$	This study
Total space velocity	V_{Tot}	+108.0	km s $^{-1}$	This study
Apogalactic radius	R_{apo}	+8.43 \pm 1.08	kpc	This study
Perigalactic radius	R_{peri}	+5.09 \pm 0.51	kpc	This study
Max. distance from the Galactic plane	z_{max}	+6.48 \pm 1.90	kpc	This study
Orbital eccentricity	e	+0.25 \pm 0.03	...	This study
Vertical angular momentum	L_Z	+0.849 \pm 0.161 $\times 10^3$	kpc km s $^{-1}$	This study
Total orbital energy	E	-1.640 \pm 0.525 $\times 10^5$	km 2 s $^{-2}$	This study

Note.

^a Using $\varpi_{\text{zp}} = -0.0434$ mas from Lindegren et al. (2021).

of Placco et al. 2022). In Almeida-Fernandes et al. (2023), four criteria for the selection of metal-poor stars from S-PLUS were proposed, resulting in different levels of completeness and purity. We note that SPLUS J1424–2542 was selected as a low-metallicity candidate in all the considered cases.

The top panel of Figure 1 shows the S-PLUS filter curves, and the 12 magnitudes (AB system) for SPLUS J1424–2542. Image cutouts for each filter (4.5 \times 4.5 centered at SPLUS J1424–2542) are shown on the right side of the figure. RGB colors are assigned based on the central wavelength of each filter. As a comparison, the S-PLUS magnitudes (scaled to the SDSS z -band value for SPLUS J1424–2542) for SPLUS J2104–0049, an ultra-metal-poor star with

[Fe/H] = -4.03 (Placco et al. 2021c), are shown. Both stars have similar temperatures, meaning that the differences in flux for the blue filters can be attributed to lower emerging flux for SPLUS J1424–2542 due to the presence of absorption features, a consequence of its overall higher chemical abundances when compared to SPLUS J2104–0049.

Medium-resolution ($R \sim 1500$) spectroscopy for SPLUS J1424–2542 was gathered on 2021 June 18, with the 8.1 m Gemini-South telescope and the GMOS (Davies et al. 1997; Gimeno et al. 2016) instrument, as part of the Poor Weather program GS-2021A-Q-419. Further details on the observing setup and data reduction are given in Placco et al. (2022). The second panel from top to bottom on

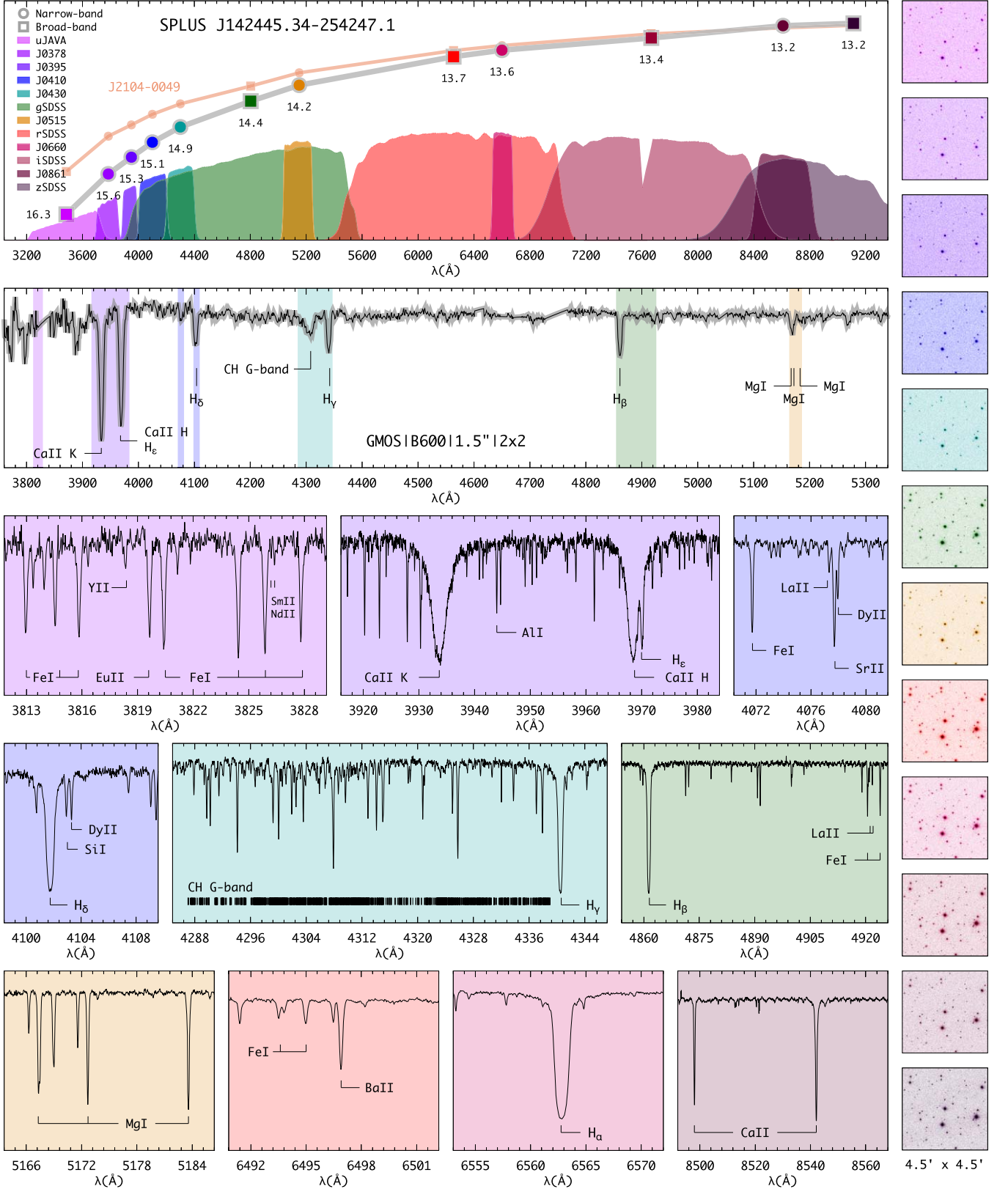


Figure 1. Top: S-PLUS magnitudes for SPLUS J1424–2542 compared to the values for SPLUS J2104–0049. Also shown are the S-PLUS filter transmission curves. The second panel from top to bottom shows the Gemini/Gemini Multi-Object Spectrograph (GMOS) spectrum, highlighting absorption features of interest. The remaining color panels show sections of the GHOST spectra and features used for the chemical abundance determinations. The 12 side panels show the S-PLUS images for SPLUS J1424–2542. The RGB colors in all panels are assigned based on the central wavelength of each filter. See text for further details.

Figure 1 shows the normalized GMOS data, highlighting a few absorption features of interest for the determination of the effective temperature (T_{eff} : Balmer lines $H\beta$, $H\gamma$, and $H\delta$,

metallicity ([Fe/H]: Ca II K), carbon abundance (CH; G band), and α -element abundance (Mg I b triplet). The atmospheric parameters determined by Placco et al. (2022) are provided in

Table 2
Atomic Data and Derived Abundances

Ion	λ (Å)	χ (eV)	$\log gf$	EW (mÅ)	$\log \epsilon(X)$	References	Δ NLTE
CH	4313.00	syn	4.83	1	...
Na I	5889.95	0.00	0.11	142.63	3.57	1	-0.37
Na I	5895.92	0.00	-0.19	118.77	3.43	1	-0.27
Mg I	3829.35	2.71	-0.23	141.24	4.80	1	0.08
Mg I	3832.30	2.71	0.25	177.79	4.72	1	0.06
Mg I	3986.75	4.35	-1.06	15.44	4.87	1	...
Mg I	4167.27	4.35	-0.74	18.56	4.64	1	0.13
Mg I	4702.99	4.33	-0.44	34.70	4.65	1	0.18
Mg I	5172.68	2.71	-0.36	156.21	4.79	1	0.05
Mg I	5183.60	2.72	-0.17	177.67	4.84	1	0.04
...

(This table is available in its entirety in machine-readable form.)

Table 1. Based on these parameters, SPLUS J1424–2542 was selected as a potential candidate for high-resolution spectroscopic follow-up.

2.2. Gemini/GHOST

SPLUS J1424–2542 was followed up in high resolution using the newly commissioned GHOST (Ireland et al. 2014; McConnachie et al. 2022; Hayes et al. 2023) at Gemini-South. Observations were conducted on 2023 May 10, as part of the GHOST System Verification²⁷ (SV; Program ID: GS-2023A-SV-101) and the data are publicly available at the Gemini Observatory Archive.²⁸ The instrument setup chosen was the standard resolution (SR: $R \sim 50,000$) and target mode IFU1:Target—IFU2:Sky. For both the blue and red cameras, six 900 s exposures were taken with 1×2 binning (spectral \times spatial). During the observations, the image quality (IQ) and cloud cover (CC) were in the 70th percentile and the sky background (SB) was in the 50th percentile.²⁹ The wavelength coverage is 3474–5438 Å for the blue camera and 5209–10608 Å for the red camera.

Data reduction was performed using v3.0 of the DRAGONS³⁰ software package (Labrie et al. 2019, 2022). This version includes support for GHOST, based on the GHOST Data Reduction pipeline v1.0 (GHOST DR; originally described in Ireland et al. 2018; Hayes et al. 2022), which was modified by the DRAGONS team during the commissioning of GHOST. The reduction steps included bias and flat corrections, wavelength calibration, sky subtraction, barycentric correction, extraction of individual orders, and variance-weighted stitching of the spectral orders. The six individual exposures were combined using a simple mean without rejection. The S/Ns per pixel achieved in selected regions of the spectrum are listed in Table 1. The colored panels on Figure 1 show sections of the GHOST data (after normalization and radial velocity shifting), highlighting absorption features of interest for the determination of stellar atmospheric parameters and chemical abundances, as described in Section 3.

²⁷ <https://www.gemini.edu/instrumentation/ghost/ghost-system-verification>

²⁸ <https://archive.gemini.edu/searchform/GS-2023A-SV-101-9/>

²⁹ Further details on the observing constraints can be found at <https://gemini.edu/observing/telescopes-and-sites/sites>

³⁰ <https://github.com/GeminiDRSoftware/DRAGONS>.

3. Atmospheric Parameters and Chemical Abundances

3.1. Atmospheric Parameters

The stellar atmospheric parameters (effective temperature T_{eff} , surface gravity $\log g$, and metallicity [Fe/H]) for SPLUS J1424–2542 were first calculated by Placco et al. (2022) using Gemini/GMOS data and the methods described therein. These parameters ($T_{\text{eff}} = 4700$ K, $\log g = 1.48$, and $[\text{Fe}/\text{H}] = -3.82$) were used to select SPLUS J1424–2542 as a potential candidate for high-resolution spectroscopic follow-up.

In this work, the T_{eff} for SPLUS J1424–2542 was calculated from the color– T_{eff} –[Fe/H] relations derived by Mucciarelli et al. (2021). We used the same procedure outlined in Roederer et al. (2018b), drawing 10^5 samples of magnitude, reddening, and metallicity. The G , BP, and RP magnitudes were retrieved from the third data release of the Gaia mission (DR3; Gaia Collaboration et al. 2023) and the K magnitude from the Two Micron All Sky Survey (2MASS; Skrutskie et al. 2006). The final $T_{\text{eff}} = 4762 \pm 36$ K is the weighted mean of the median temperatures for each input color (BP – RP, BP – G , G – RP, BP – K , RP – K , and G – K). The $\log g$ was calculated using Equation (1) in Roederer et al. (2018b), drawing 10^5 samples from the input parameters listed in Table 1. The final $\log g = 1.58 \pm 0.11$ is taken as the median of those calculations with the uncertainty given by their standard deviation.

The metallicity was determined spectroscopically from the equivalent widths (EWs) of 104 Fe I lines in the GHOST spectrum by fixing the T_{eff} and $\log g$ determined above. Table 2 lists the lines employed in this analysis, their measured EWs, and the derived chemical abundances. The EWs were obtained by fitting Gaussian profiles to the observed absorption features using standard IRAF³¹ routines, then [Fe/H] was calculated using the latest version of the MOOG³² code (Sneden 1973), employing one-dimensional plane-parallel model atmospheres with no overshooting (Castelli & Kurucz 2004), assuming local thermodynamic equilibrium (LTE). The microturbulent velocity (ξ) was determined by minimizing the trend between the Fe I abundances and their reduced EWs ($\log(\text{EW}/\lambda)$). The final

³¹ IRAF was distributed by the National Optical Astronomy Observatory, which was managed by the Association of Universities for Research in Astronomy (AURA) under a cooperative agreement with the National Science Foundation.

³² <https://github.com/alexji/moog17scat>

Table 3
LTE Abundances for Individual Species

Species	$\log \epsilon_{\odot}(X)$	$\log \epsilon(X)$	(X/H)	(X/Fe)	σ	N
C	8.43	4.83	-3.60	-0.21	0.10	1
C ^a	8.43	5.10	-3.33	0.06	0.10	1
Na I	6.24	3.50	-2.74	0.65	0.07	2
Mg I	7.60	4.75	-2.85	0.54	0.07	9
Al I	6.45	2.80	-3.65	-0.26	0.15	1
Si I	7.51	4.76	-2.75	0.64	0.15	1
Ca I	6.34	3.36	-2.98	0.41	0.08	11
Sc II	3.15	-0.02	-3.17	0.22	0.05	7
Ti I	4.95	1.70	-3.25	0.14	0.05	7
Ti II	4.95	1.94	-3.01	0.38	0.09	20
V II	3.93	0.97	-2.96	0.43	0.02	2
Cr I	5.64	1.79	-3.85	-0.46	0.10	3
Mn I	5.43	1.51	-3.92	-0.53	0.09	3
Fe I	7.50	4.11	-3.39	0.00	0.12	104
Fe II	7.50	4.19	-3.31	0.08	0.04	11
Co I	4.99	1.68	-3.31	0.08	0.06	3
Ni I	6.22	2.74	-3.48	-0.09	0.15	1
Zn I	4.56	1.36	-3.20	0.19	0.15	1
Sr II	2.87	0.37	-2.50	0.89	0.10	2
Y II	2.21	-0.74	-2.95	0.44	0.04	6
Zr II	2.58	-0.20	-2.77	0.62	0.04	4
Ba II	2.18	0.04	-2.14	1.25	0.10	3
La II	1.10	-1.01	-2.11	1.28	0.06	8
Ce II	1.58	-0.63	-2.21	1.18	0.06	10
Pr II	0.72	-1.15	-1.87	1.52	0.02	3
Nd II	1.42	-0.58	-2.00	1.39	0.04	22
Sm II	0.96	-0.92	-1.88	1.51	0.08	17
Eu II	0.52	-1.25	-1.77	1.62	0.05	8
Gd II	1.07	-0.74	-1.81	1.58	0.04	9
Tb II	0.30	-1.35	-1.65	1.74	0.20	1
Dy II	1.10	-0.47	-1.57	1.82	0.12	9
Ho II	0.48	-1.33	-1.81	1.58	0.08	3
Er II	0.92	-0.80	-1.72	1.67	0.06	4
Tm II	0.10	-1.65	-1.75	1.65	0.08	4
Yb II	0.84	-1.06	-1.90	1.49	0.20	1
Hf II	0.85	-1.15	-2.00	1.39	0.20	1
Os I	1.40	-0.21	-1.61	1.78	0.04	2
Ir I	1.38	-0.35	-1.73	1.66	0.20	1
Th II	0.02	-1.21	-1.23	2.16	0.06	3

Note.

^a Using the carbon evolutionary corrections of Placco et al. (2014).

atmospheric parameters for SPLUS J1424–2542 are listed in Table 1.

3.2. Chemical Abundances

The GHOST spectrum allowed for the detection of 308 absorption features for 36 elements, spanning the wavelength range $3694 \leq \lambda(\text{\AA}) \leq 8807$. Abundances were determined from an EW analysis and spectral synthesis, both using MOOG. These features and their atomic data are listed in Table 2. Line lists for each abundance determination through spectral synthesis were generated using the linemake code³³ (Placco et al. 2021a, 2021b). Logarithmic abundances by number ($\log \epsilon(X)$) and abundance ratios ([X/H] and [X/Fe]), were calculated adopting the solar photospheric abundances ($\log \epsilon_{\odot}(X)$) from Asplund et al. (2009). The average abundances and the number of lines measured (N) for each element

³³ <https://github.com/vmplacco/linemake>

Table 4
Example Systematic Abundance Uncertainties for SPLUS J1424–2542

Elem	ΔT_{eff} +150 K	$\Delta \log g$ +0.3 dex	$\Delta \xi$ +0.3 km s ⁻¹	σ	σ_{tot}
Na I	0.18	-0.06	-0.13	0.07	0.24
Mg I	0.13	-0.06	-0.05	0.07	0.17
Ca I	0.10	-0.02	-0.02	0.08	0.13
Sc II	0.09	0.07	-0.03	0.05	0.13
Ti I	0.18	-0.02	-0.02	0.05	0.19
Ti II	0.08	0.08	-0.05	0.09	0.15
Cr I	0.19	-0.03	-0.08	0.10	0.23
Mn I	0.22	-0.03	-0.13	0.09	0.27
Fe I	0.16	-0.02	-0.04	0.12	0.20
Fe II	0.02	0.08	-0.01	0.04	0.09
Co I	0.20	-0.02	-0.07	0.06	0.22
Ni I	0.17	-0.01	-0.02	0.15	0.23

are given in Table 3. The σ values are the standard error of the mean. For elements with only one line measured, the uncertainty was estimated by minimizing the residuals between the GHOST data and a set of synthetic spectra through visual inspection.

We have also quantified the systematic uncertainties due to changes in the atmospheric parameters for elements with $6 < Z \leq 30$ using the abundances determined by the EW analysis only (see details below), following the prescription described in Placco et al. (2013, 2015b). Table 4 shows the derived abundance variations when each atmospheric parameter is varied within the quoted uncertainties. Also listed is the total uncertainty for each element, calculated from the quadratic sum of the individual error estimates. The adopted variations for the parameters are +150 K for T_{eff} , +0.3 dex for $\log g$, and +0.3 km s⁻¹ for ξ .

3.2.1. From C to Zn

Apart from C, Al, Si, V, and Zn, all the abundances for elements with $Z \leq 30$ were measured from the EWs. The carbon abundance was determined from the CH G-band spectral synthesis, assuming $^{12}\text{C}/^{13}\text{C} = 4$. Figure 2 shows the GHOST spectrum (filled squares) compared to the synthetic data. The red solid line shows the best-fit synthesis and the shaded regions at ± 0.1 and ± 0.2 dex are used to determine the uncertainty. Also shown is a synthetic spectrum after removing all contributions from carbon (gray line). The carbon depletion on the giant branch for SPLUS J1424–2542 (+0.27 dex) was determined using the procedures described by Placco et al. (2014).³⁴

For the remaining light elements, there is overall good agreement among the abundances of individual lines for a given species, which can be seen from the small σ values listed in Table 3. We have also obtained non-LTE (NLTE) corrections for 157 absorption features in the spectrum of SPLUS J1424–2542, using INSPECT³⁵ (Na I), Nordlander & Lind (2017; Al I), and MPIA NLTE³⁶ (Mg I, Si I, Ca I, Ti I, Ti II, Cr I, Mn I, Fe I, and Co I). Literature references are given in Table 2 along with the corrections for individual lines in the last column. Average NLTE abundances, abundance ratios, and

³⁴ <https://vplacco.pythonanywhere.com/>

³⁵ <http://www.inspect-stars.com/>

³⁶ <https://nlte.mpi.de/>

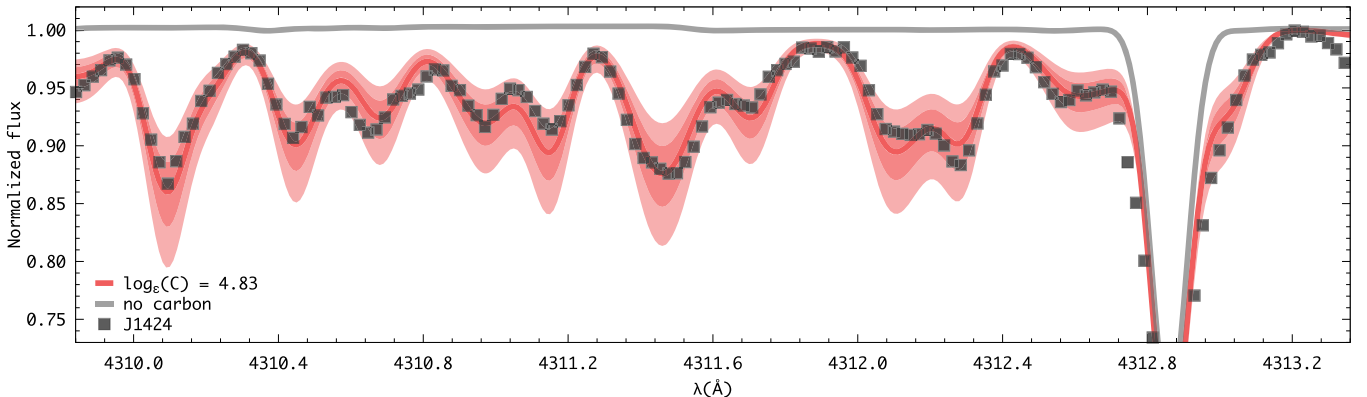


Figure 2. Spectral synthesis for the determination of the carbon abundance. The red solid line shows the best-fit synthesis and uncertainties (± 0.1 and ± 0.2 dex—shaded regions) compared to the observed spectra (filled squares). Also shown is a synthetic spectrum after removing all contributions from carbon (gray line).

σ values are given in Table 5. The average NLTE corrections range from -0.32 for Na I to $+1.0$ for Al I, with notably high corrections also for Cr I and Co I ($+0.79$ and $+0.70$, respectively). Due to the overall low metallicity (and low carbon abundance) of SPLUS J1424–2542, most lines have a well-defined continuum and are not blended with other species (see, for example, Mg I and Ca II in the lower panels of Figure 1). Unless otherwise noted, we use the LTE abundances from Table 3 for the remainder of this work.

3.2.2. From Sr to Th

The spectral synthesis of 121 absorption features was conducted for 21 chemical species with $Z \geq 38$ and summarized in Table 3. Where appropriate, we accounted for line broadening by isotopic shifts and hyperfine splitting structure. For all syntheses, we fixed the abundances of carbon, iron, and the $^{12}\text{C}/^{13}\text{C}$ ratio. We also used the r -process isotopic fractions from Sneden et al. (2008) for specific elements, as described below. Figures 3 and 4 show the spectral synthesis for selected heavy elements. The symbols and lines have the same meaning as those shown in Figure 2.

Strontium, yttrium, and zirconium. For these first-peak elements, there is excellent agreement between the abundances of individual lines. Both Sr lines ($\lambda 4077$ and $\lambda 4215$) were fit with the same abundance ($\log \epsilon(\text{Sr}) = 0.37$) and the spread is small for the six Y lines (0.12 dex) and four Zr lines (0.10 dex). The synthesis for one of the Y lines is shown in Figure 3.

Barium and lanthanum. These second-peak elements have low r -process fractions (Ba: 15%; La: 25%; Burris et al. 2000) in the solar system. For Ba, the strongest lines ($\lambda 4554$ and $\lambda 4934$) appear saturated and were not considered in the analysis. The three Ba lines measured at redder wavelengths agree within 0.20 dex, with an average $\log \epsilon(\text{Ba}) = +0.04$. For La, the eight lines measured also agree within 0.20 dex, with an average of $\log \epsilon(\text{La}) = -1.01$. The syntheses for the Ba ($\lambda 6141$) and La ($\lambda 4086$, including hyperfine splitting) lines are shown in Figure 3.

Cerium, praseodymium, neodymium, and samarium. These elements have a large number of lines identified at wavelengths $\lambda \leq 4600$ Å (see Roederer et al. 2018b, for a comprehensive list). In total, 52 lines were measured in the GHOST spectrum of SPLUS J1424–2542, with standard deviations $\sigma \leq 0.08$. Figure 4 shows the synthesis for two Sm lines and Figure 3

Table 5
NLTE Abundances for Individual Species

Species	$\log \epsilon_{\odot}(\text{X})$	$\log \epsilon(\text{X})$	[X/H]	[X/Fe]	σ	N
Na I	6.24	3.18	-3.06	0.15	0.03	2
Mg I	7.60	4.83	-2.77	0.44	0.05	8
Al I	6.45	3.80	-2.65	0.51	0.15	1
Si I	7.51	4.79	-2.72	0.51	0.15	1
Ca I	6.34	3.64	-2.70	0.41	0.07	9
Ti I	4.95	2.30	-2.65	0.56	0.06	6
Ti II	4.95	2.04	-2.91	0.30	0.10	19
Cr I	5.64	2.49	-3.15	0.06	0.06	3
Mn I	5.43	1.83	-3.60	-0.39	0.08	3
Fe I	7.50	4.29	-3.21	0.00	0.13	102
Co I	4.99	2.47	-2.52	0.69	0.02	3

Note. The complete list of literature references for the NLTE corrections is given in Table 2.

shows the synthesis for Ce and Pr (including hyperfine splitting).

Eu. Eu is one of the most widely used elements to indicate r -process nucleosynthesis and it is used to classify stars into various categories for heavy-element signatures (Frebel 2018). Eight lines were measured in the GHOST spectrum, ranging from $\lambda 3724$ ($\log \epsilon(\text{Eu}) = -1.17$) to $\lambda 6645$ ($\log \epsilon(\text{Eu}) = -1.23$). Two examples of the Eu spectral synthesis are shown in Figure 3 ($\lambda 4205$) and Figure 4 ($\lambda 4435$). In both cases, there is overall good agreement between the observations (filled symbols) and the best synthetic fit (red lines). The final average is $\log \epsilon(\text{Eu}) = -1.25$ ($[\text{Eu}/\text{Fe}] = +1.62$).

Gadolinium, terbium, dysprosium, holmium, erbium, thulium, ytterbium, and hafnium. These elements, with $64 \leq Z \leq 72$, are mostly formed by the r -process, according to the fractions in Burris et al. (2000). In total, 32 lines were measured within this group (most at $\lambda \leq 4000$ Å), with only one feature each for Tb ($\lambda 3874$), Yb ($\lambda 3694$), and Hf ($\lambda 4093$). There were nine Dy lines measured with a somewhat high dispersion ($\sigma = 0.12$ dex) and good agreement for Gd (nine lines, $\sigma = 0.04$), Ho (three lines, $\sigma = 0.08$), Er (four lines, $\sigma = 0.06$), and Tm (four lines, $\sigma = 0.08$). The top panels of Figure 3 show the syntheses for the Tm ($\lambda 3795$) and Er ($\lambda 3896$) lines.

Osmium and iridium. These third-peak elements are almost exclusively formed by the r -process in the solar system

Table 6
Information for the Literature Comparison Sample in Figure 8

Star	[Fe/H]	$\log \epsilon$ (Eu)	$\log \epsilon$ (Th)	Reference
LAMOST J112456.61+453531.3	-1.27	0.35	-0.16	Xing et al. (2019)
HD 222925	-1.47	0.38	-0.06	Roederer et al. (2008)
COS82	-1.47	0.34	-0.25	Aoki et al. (2007)
RAVE J093730.5–062655	-1.86	-0.49	-0.79	Sakari et al. (2019)
2MJ1521–0607	-2.00	-0.55	-1.36	Sakari et al. (2018a)
BD+173248	-2.06	-0.67	-1.18	Cowan et al. (2002)
RAVE J153830.9–180424	-2.09	-0.32	-0.97	Sakari et al. (2018b)
HD 221170	-2.16	-0.86	-1.46	Ivans et al. (2006)
2MJ2256–0719	-2.26	-0.64	-1.46	Sakari et al. (2018a)
2MASS J21511791–1233417	-2.37	0.17	-0.50	Cohen et al. (2003)
2MASS J15141890+0727028	-2.41	-1.02	-1.12	Honda et al. (2004)
J0246–1518	-2.45	-0.64	-1.40	Sakari et al. (2018a)
HD 108317	-2.53	-1.37	-1.99	Roederer et al. (2012)
2MASS J22310218–3238365	-2.60	-1.03	-1.43	Hayek et al. (2009)
2MASS J00280692–2603042	-2.68	-0.45	-0.90	Christlieb et al. (2004a)
2MASS J23303707–5626142	-2.78	-1.29	-1.67	Mashonkina et al. (2010b)
J1521–3538	-2.80	-0.05	-0.60	Cain et al. (2018)
BD–16251	-2.80	-0.59	-0.92	Honda et al. (2004)
CS 29497–004	-2.85	-0.65	-1.23	Hill et al. (2017)
RAVE J203843.2–002333	-2.91	-0.75	-1.24	Placco et al. (2017)
2MASS J22545856–4209193	-2.94	-1.30	-1.63	Mashonkina et al. (2014b)
HD 115444	-2.96	-1.63	-2.23	Westin et al. (2000)
J1432–4125	-2.97	-1.01	-1.47	Cain et al. (2018)
2MASS J12213413–0328396	-2.97	-1.06	-1.29	Hayek et al. (2009)
2MASS J09544277+5246414	-2.99	-1.19	-1.31	Holmbeck et al. (2018)
TYC 5594–576–1	-3.00	-0.62	-1.20	Frebel et al. (2007)
DES J033523–540407	-3.00	-0.93	-1.77	Ji & Frebel (2018)
J2005–3057	-3.03	-1.57	-2.17	Cain et al. (2018)
2MASS J22170165–1639271	-3.10	-0.95	-1.57	Sneden et al. (2003)
2MASS J01021585–6143458	-3.13	-1.69	-1.92	Roederer et al. (2014)
LAMOST J1109+0754	-3.17	-1.71	-2.05	Mardini et al. (2020)
SPLUS J142445.34–254247.1	-3.39	-1.25	-1.21	This work
2MASS J23342669–2642140	-3.43	-2.24	-2.45	Siqueira Mello et al. (2014)

(Os: 92%; Ir: 99%; Burris et al. 2000) and also do not have many lines available for abundance determination in the spectral range of the GHOST data. The abundances for the two Os lines ($\lambda 4260$ and $\lambda 4420$) agree within 0.07 dex, with an average of $\log \epsilon(\text{Os}) = -0.21$. Only one Ir line was identified for SPLUS J1424–2542 ($\lambda 3800$), with an abundance of $\log \epsilon(\text{Ir}) = -0.35$.

Thorium. As a radioactive actinide with $Z=90$, Th is the second heaviest element with abundances measured in stellar spectra. For SPLUS J1424–2542, three lines were identified in the GHOST spectrum: $\lambda 4019$ ($\log \epsilon(\text{Th}) = -1.13$), $\lambda 4086$ ($\log \epsilon(\text{Th}) = -1.23$), and $\lambda 4094$ ($\log \epsilon(\text{Th}) = -1.28$). Their spectral syntheses are shown in Figure 3. For the $\lambda 4019$ line, the abundances of C, Fe, Ni, Ce, and Nd were held constant using the average values in Table 3, and there appears to be a reduction artifact on the blue wing of the Th line. The La abundance was also held constant for the $\lambda 4086$ synthesis. The GHOST spectrum was slightly smoothed (with a moving average of size 5 pixels) for the synthesis of the $\lambda 4094$ line. The final average is $\log \epsilon(\text{Th}) = -1.21$.

4. The Chemo-dynamical Nature of SPLUS J1424–2542

In this section, we discuss the chemo-dynamical nature of SPLUS J1424–2542 by comparing its chemical abundance pattern with Population III supernova nucleosynthesis yields ($Z \leq 30$), the *r*- and *s*-process solar fractions, and predictions from a simulation of neutron star mergers ($Z \geq 38$). We also

determine the mass, age, and orbit of SPLUS J1424–2542, in an attempt to constrain its formation history.

4.1. The Light-element Abundance Pattern

At $[\text{Fe}/\text{H}] = -3.39$, $[\text{C}/\text{Fe}] = +0.06$, and with enhancements in heavy elements, SPLUS J1424–2542 most likely was formed from a gas cloud polluted by at least two progenitor populations. To corroborate that hypothesis, the $[\text{Mg}/\text{C}]$ abundance ratio from Hartwig et al. (2018) can be used as a diagnostic to distinguish between mono- and multienriched stars. For SPLUS J1424–2542, both the observed and natal values ($[\text{Mg}/\text{C}] = +0.75$ and $+0.48$, respectively) are consistent with the multienriched classification (Figure 11 of Hartwig et al. 2018).

Nonetheless, we can attempt to infer the main features of the progenitor population that enriched the gas cloud that formed SPLUS J1424–2542 with elements from carbon to zinc. We modeled the light-element abundance signature of SPLUS J1424–2542 by comparing it with the theoretical Population III supernova nucleosynthesis yields³⁷ from Heger & Woosley (2010). These models predict the nucleosynthesis products of massive metal-free stars with pristine Big Bang nucleosynthesis initial composition, without mass loss and rotation throughout the evolution. The fallback models (S4) used in this work have masses from 10 to 100 M_{\odot} and

³⁷ <http://starfit.org>

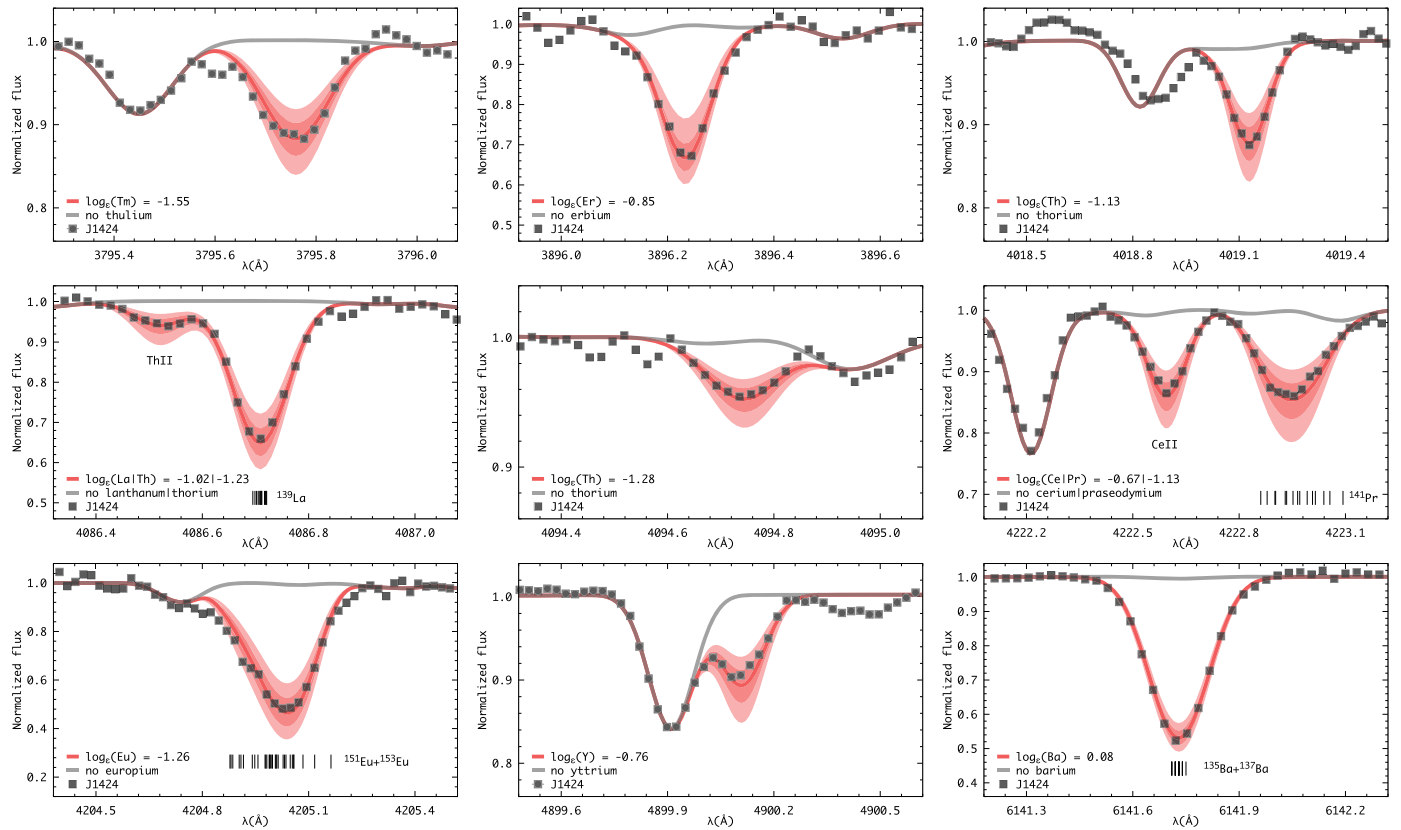


Figure 3. Same as Figure 2, for the heavy elements highlighted in each panel.

explosion energies ranging from 0.3×10^{51} erg to 10×10^{51} erg. The comparison between models and observations, as well as the χ^2 matching algorithm, has already been applied to extremely metal-poor stars in the literature (Frebel et al. 2015; Roederer et al. 2016; Placco et al. 2020; among others) and provides important constraints on the progenitor population of second-generation stars.

Similar to Placco et al. (2016), we created 10,000 abundance patterns for SPLUS J1424–2542 by resampling the $\log \epsilon(X)$ and σ values from Table 3. By determining the best-fit model for each resampled pattern using the LTE abundances, we found that 36 unique models provided an acceptable fit for at least 10 resamples. The results of this exercise are shown in Figure 5. In the upper panel, the filled circles show the chemical abundances for SPLUS J1424–2542 and the lines represent the different models used for the fitting. The labels show the percentage occurrence for the most frequent models among the 10,000 runs. The bottom panel shows the residuals between observations and the three most frequent models.

The “best-fit” result found in 49% of the resamples is a model with $13.4 M_{\odot}$ [$0.9\text{--}1.2 \times 10^{51}$ erg], followed by $11.3 M_{\odot}$ [$0.6\text{--}0.9 \times 10^{51}$ erg] in 41% of the resamples. There is overall good agreement between the two best-fit models and the observed abundances for SPLUS J1424–2542, with somewhat large ($\geq +0.3$ dex) residuals for carbon and chromium. It is interesting to note that, out of the 10,000 resamples, about 90% have their best-fit model for either $13.4 M_{\odot}$ or $11.3 M_{\odot}$ within a narrow range of explosion energies.

We repeated this exercise for the NLTE abundances in Table 5 and the results are shown in Figure 6. For the set of 10 elements (as opposed to 15 in LTE), the most likely Population

III characteristics are very similar to the LTE case, with a preference for lower masses and explosion energies. For 34% of the resamples, $10.6 M_{\odot}$ progenitors provide the best fit, followed by the $11.3 M_{\odot}$ (33%) and $10.2 M_{\odot}$ (28%) models, all with explosion energies within $0.3\text{--}1.8 \times 10^{51}$ erg. Even though these results agree well with the LTE analysis, it is worth pointing out that carbon (and nitrogen) are key elements when comparing observations with the faint-supernova models, as pointed out by Placco et al. (2015a). Additional abundance determinations and NLTE corrections would help further constrain these models.

For both the LTE and NLTE abundance patterns, this exercise suggests that a progenitor star on the low-mass end of the supernovae grid with low explosion energy could be responsible for the light-element abundance pattern of SPLUS J1424–2542. This mass range and explosion energies are not consistent with the progenitor population suggested for stars with similar low carbon abundances: $30 M_{\odot}$ for SPLUS J2104–0049 (Placco et al. 2021a) and $20 M_{\odot}$ for AS0039 (Skúladóttir et al. 2021), both with an explosion energy of 10×10^{51} erg. This may be a metallicity effect since these stars are in the $[\text{Fe}/\text{H}] < -4$ regime, so further exploration of the progenitor population of extremely metal-poor stars would help better constrain their main characteristics.

4.2. The Heavy-element Abundance Pattern

With $[\text{Eu}/\text{Fe}] = +1.62$ and $[\text{Ba}/\text{Eu}] = -0.37$ abundance ratios, SPLUS J1424–2542 is classified as an *r*-II metal-poor star (Frebel 2018), with a clear signature of the main *r*-process. Its heavy-element abundance pattern, compared to the solar

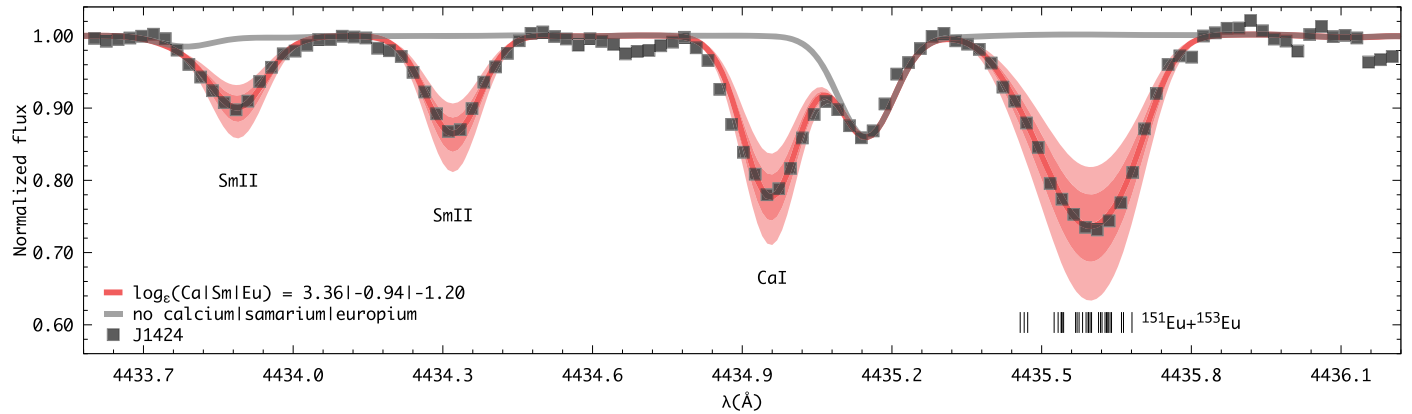


Figure 4. Same as Figure 2 for the samarium, calcium, and Eu abundance determinations.

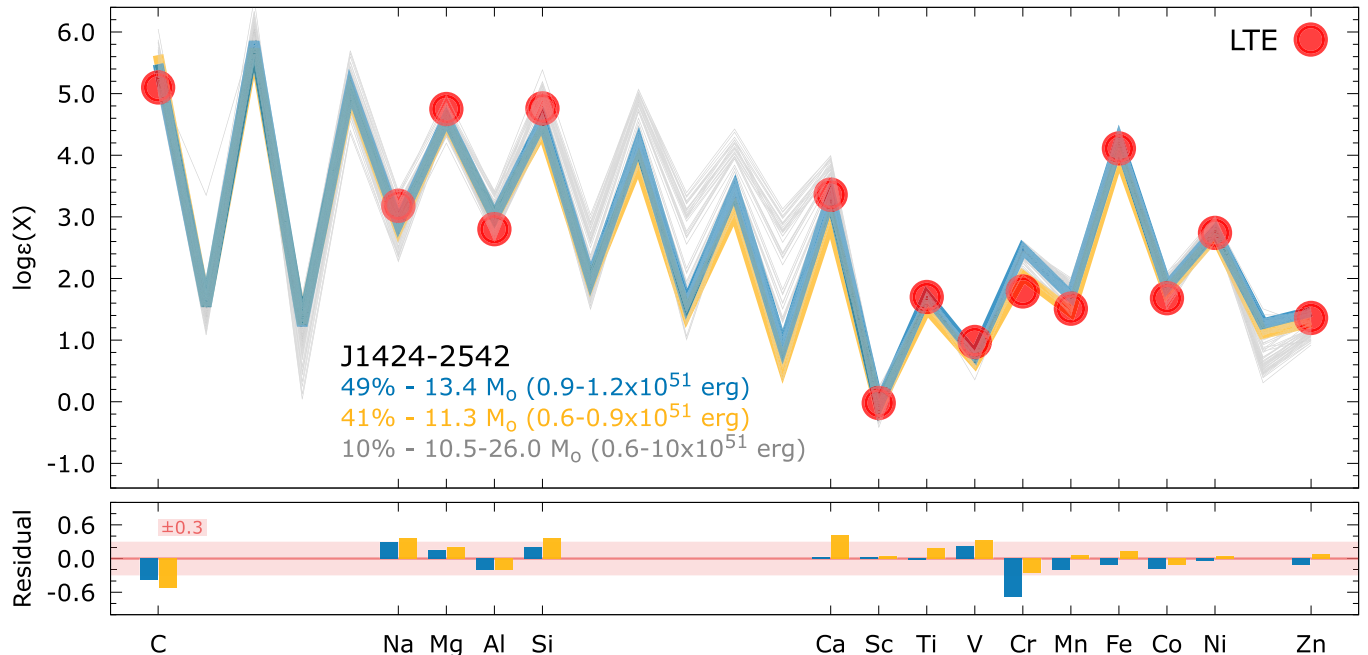


Figure 5. Upper panel: light-element chemical abundance pattern of SPLUS J1424–2542, (filled circles, LTE) compared with the yields from metal-free supernova models (solid lines). The labels show the progenitor mass and explosion energy of the models and their percentage occurrence among the 10,000 abundance pattern resamples of SPLUS J1424–2542. Lower panel: residuals between the observations and the two best-fit models. A ± 0.3 dex shaded area is shown for reference.

system *s*-process (scaled to Ba) and *r*-process (scaled to Eu), is shown in the upper panel of Figure 7. Filled circles are the average abundance for each element, while empty circles show the abundances for all the lines measured in the GHOST spectrum. Each label shows the element symbol and its *s* and *r* fractions, taken from Burris et al. (2000). Also shown are the number of lines used to calculate the average abundance for each element. The lower panel shows the residuals between observations and the scaled patterns. For reference, the red shaded area denotes the typical uncertainty (~ 0.2 dex) in the abundance measurements.

Sr, Y, and Zr agree with neither the scaled *s* nor *r* patterns for SPLUS J1424–2542. These elements are formed mainly by the *s*-process in the stars whose metals enriched the Sun. However, there are a number of possible formation channels for these light neutron-capture elements (dubbed “limited” *r*-process), which could help explain their large variation when compared with the normalized *r*-process patterns among low-metallicity stars (see Table 2 and Figure 5 in Frebel 2018). For Ba, La, and Ce, there is a clear overproduction when compared to the

scaled *r*-process pattern, which could suggest a contribution from the *s*-process to the observed abundance pattern of SPLUS J1424–2542. This contribution would be revealed by abundance ratios such as [Ba/Eu] and [La/Eu], which are expected to be $\gtrsim 0.0$ if an *s*-process component is present (Roederer et al. 2010; Frebel 2018). For SPLUS J1424–2542, both ratios are consistent with the *r*-process expectation (and [Ba/Eu] = -0.37 and [La/Eu] = -0.34).

In contrast, the abundances for elements from Pr to Ir well reproduce the normalized *r*-process pattern, mostly within 1σ (with the exception of Dy). Apart from those, thorium has a measured abundance that is over 0.5 dex higher than the normalized *r*-process pattern. This “actinide-boost” phenomenon is shared by about a quarter of metal-poor stars with measurable Th (and U), and it could be evidence of either a contribution from a separate *r*-process event or small variations of neutron richness within the same type of *r*-process event that contributed to the abundance make up of SPLUS J1424–2542 (Holmbeck et al. 2018, 2019).

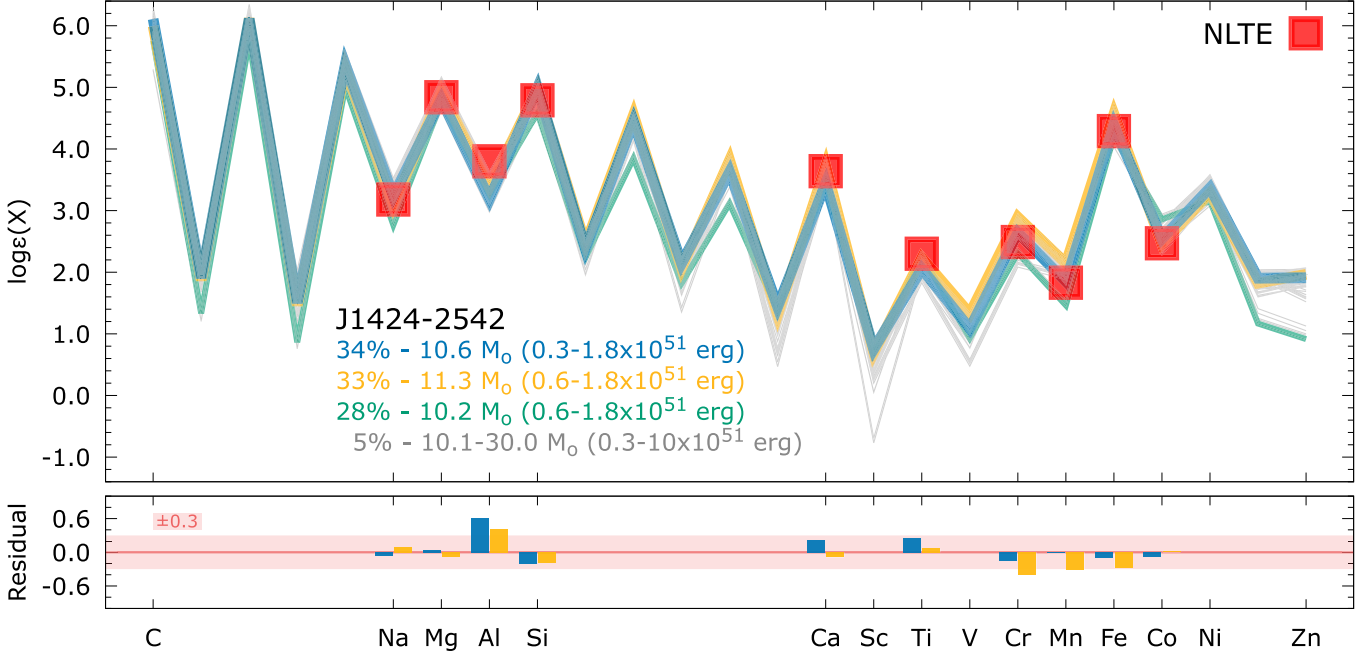


Figure 6. Same as Figure 5, using the NLTE abundances listed in Table 5.

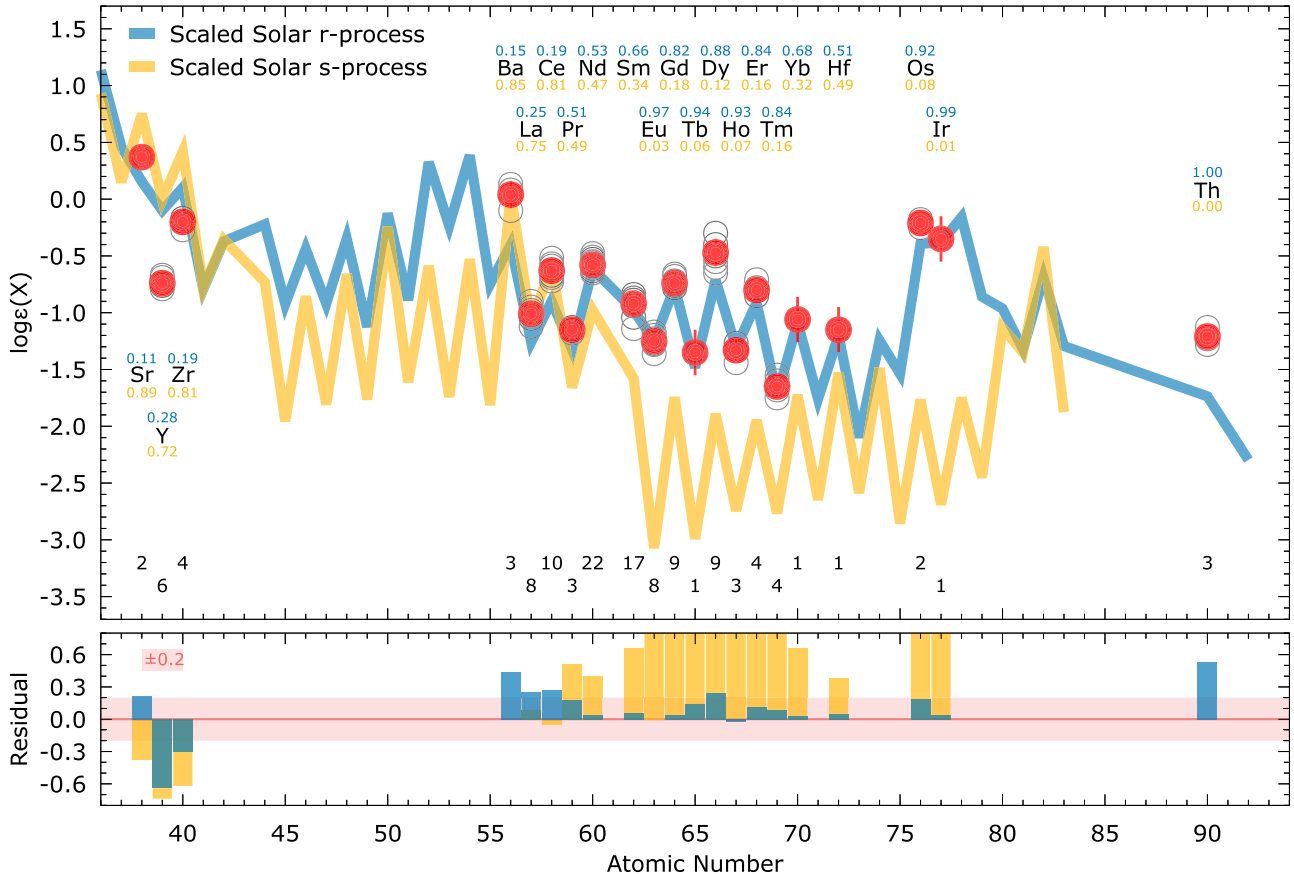


Figure 7. Upper panel: heavy-element chemical abundance pattern of SPLUS J1424–2542, compared with the scaled solar system abundances. The *r*- and *s*-process contributions are calculated based on the fractions given by Burris et al. (2000) and scaled to match the observed abundances of Eu and Ba, respectively. Also shown are the *r*- and *s*-process fractions for each element (top), as well as the number of lines identified for each element (bottom). Open circles show the individual abundances for all the lines measured in the GHOST spectrum. Lower panel: residuals between the observations and the scaled solar system abundance patterns. A ± 0.2 dex shaded area is shown for reference.

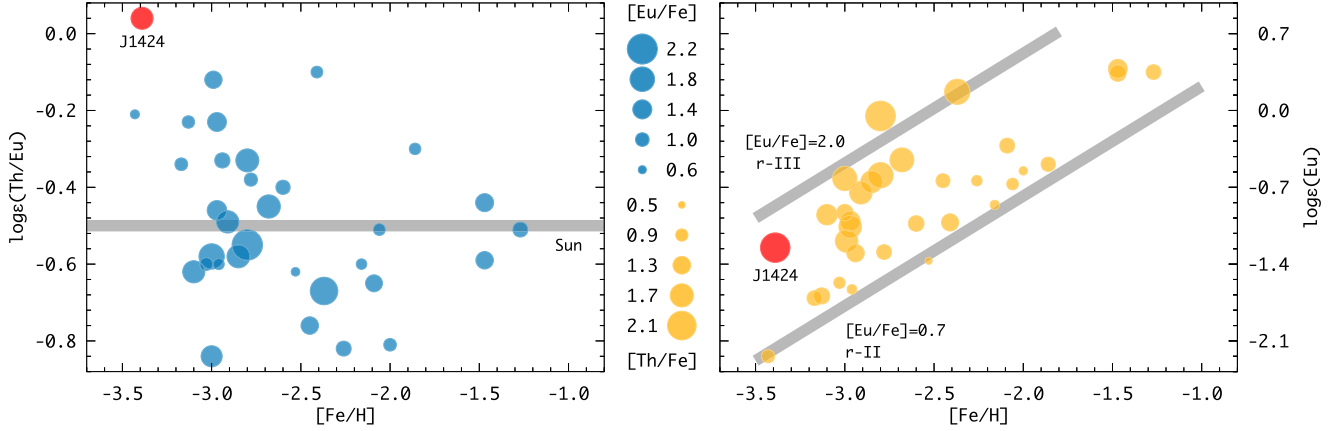


Figure 8. $\log \epsilon(\text{Th/Eu})$ (left panel) and $\log \epsilon(\text{Eu})$ (right panel) as a function of $[\text{Fe}/\text{H}]$ for metal-poor stars in the literature with both Th and Eu measured ($[\text{Fe}/\text{H}] \leq -1.0$ and $[\text{Eu}/\text{Fe}] \geq +0.60$), compared to SPLUS J1424–2542. The point sizes are proportional to $[\text{Eu}/\text{Fe}]$ (left) and $[\text{Th}/\text{Fe}]$ (right), according to the labels between the panels. The horizontal solid gray line marks the solar $\log \epsilon(\text{Th/Eu})$ value and on the right panel, the limits for the $r\text{-II}$ and $r\text{-III}$ stars are shown. Individual references are given in Table 6.

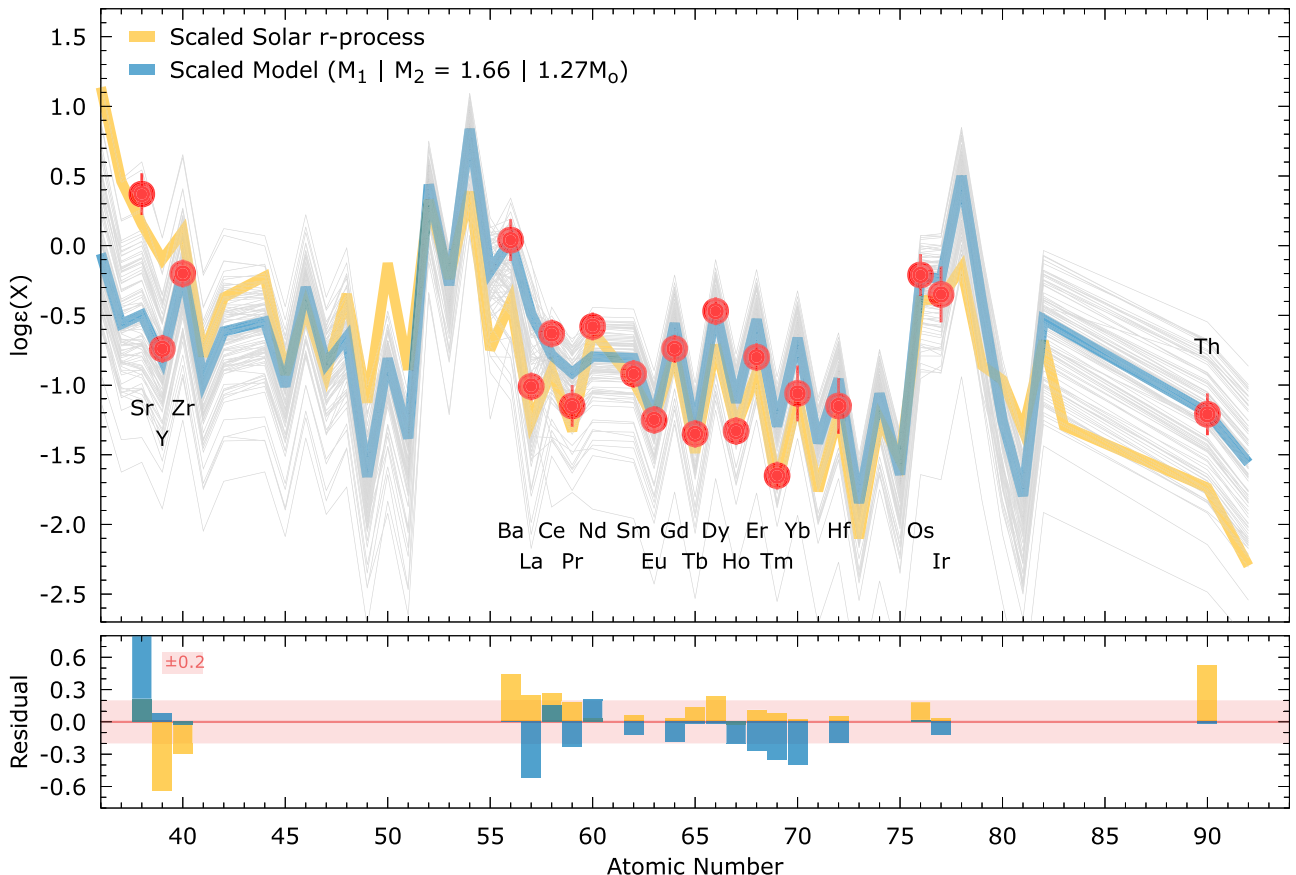


Figure 9. Upper panel: heavy-element chemical abundance pattern of SPLUS J1424–2542, compared with the scaled solar system r -process (yellow) and the best-fit neutron star merger model (blue), normalized to match the observed Eu abundance. Also shown (gray lines) are random realizations of the neutron star merger; see text for details. Lower panel: residuals between the observations and scaled predictions. A ± 0.2 dex shaded area is shown for reference.

Figure 8 shows the heavy-element abundance ratio $\log \epsilon(\text{Th/Eu})$ (left panel) and $\log \epsilon(\text{Eu})$ (right panel) as a function of $[\text{Fe}/\text{H}]$ for stars in the literature³⁸ with $[\text{Fe}/\text{H}] \leq -1.0$, $[\text{Eu}/\text{Fe}] \geq +0.6$, and both Th and Eu measured,

compared to SPLUS J1424–2542. The point sizes are proportional to $[\text{Eu}/\text{Fe}]$ (left) and $[\text{Th}/\text{Fe}]$ (right). From the left panel, it is possible to see that SPLUS J1424–2542 has the highest $\log \epsilon(\text{Th/Eu})$ within this group (well above the solar value—solid gray line) and the second lowest $[\text{Fe}/\text{H}]$, which corroborate with the hypothesis that it belongs to the “actinide-boost” category and that its heavy elements have

³⁸ Taken from the JINAbase compilation (Abohalima & Frebel 2018). Individual references are given in Table 6.

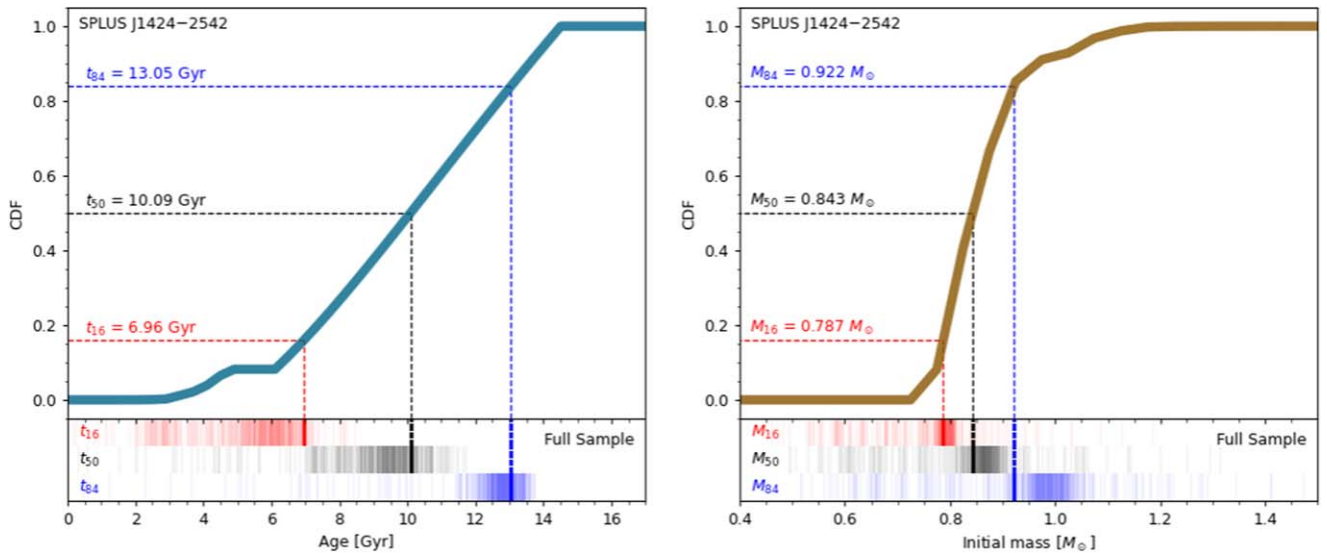


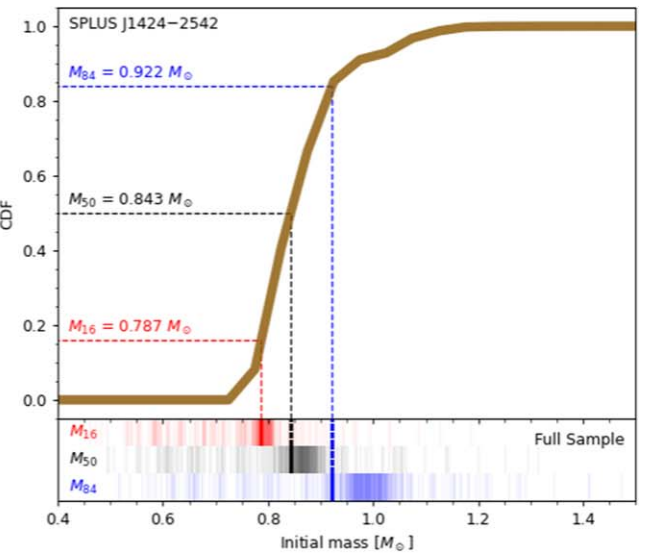
Figure 10. Age (left) and initial mass (right) CDFs obtained for SPLUS J1424–2542 using the Bayesian isochronal method described in Almeida-Fernandes et al. (2023). The dashed lines correspond to the 16th (red), 50th (black), and 84th (blue) percentiles used to characterize the parameters and their uncertainties. For comparison, the ticks in the bottom panels correspond to the 16th (red), 50th (black), and 84th (blue) percentiles for all 522 stars in the Placco et al. (2022) sample.

been produced by an *r*-process event without contributions from the *s*-process. The right panel also reveals that SPLUS J1424–2542 has one of the highest [Th/Fe] ratios and the lowest metallicity among the *r*-II stars, and similar [Th/Fe] to the *r*-III star ([Eu/Fe] $\geq +2.0$) from Cain et al. (2020). In the following section, we present one possible scenario that can explain the heavy-element abundance pattern in SPLUS J1424–2542.

4.3. Comparison with Yields from Neutron Star–Neutron Star Merger Events

Similar to the exercise in Section 4.1 for the light elements, we explore the origin of the heavy elements in SPLUS J1424–2542 made by the *r*-process. Specifically, we use the analytic model of Holmbeck et al. (2021) to find which neutron star mergers can reproduce the observed abundance pattern of SPLUS J1424–2542. This model predicts the total *r*-process yield for a neutron star merger using the neutron star masses and a nuclear equation of state (which determines their stellar radii) as input. The total *r*-process yield is found by assuming a two-component ejecta scheme with “wind” and “dynamical” components. The ejecta masses and compositions of the two components are calculated following the procedure and default model assumptions in Holmbeck et al. (2021), namely that the ejecta masses of the wind and dynamical components follow the descriptions in Dietrich et al. (2020) and Krüger & Foucart (2020), respectively. We require the model output to match the relative light-to-heavy and actinide-to-heavy abundance features present in the abundance pattern of SPLUS J1424–2542, represented by the observational $\log \epsilon(\text{Zr/Dy})$ and $\log \epsilon(\text{Th/Dy})$ abundance ratios. Using the nuclear equation of state proposed by Holmbeck et al. (2022), we find that a $1.66\text{--}1.27 M_\odot$ neutron star merger best reproduces these abundance ratios.

Including the observational uncertainties, the neutron star masses can vary within $\pm 0.02 M_\odot$ and still be able to match the elemental abundances of SPLUS J1424–2542. The model predicts median masses and lanthanide mass fractions of $m_{\text{disk}} = 7.15^{+2.96}_{-2.50} \times 10^{-3} M_\odot$ with $X_{\text{disk}}^{\text{lan}} = 0.050^{+0.019}_{-0.017}$ and



$m_{\text{dyn}} = 11.79^{+1.40}_{-1.64} \times 10^{-3} M_\odot$ with $X_{\text{dyn}}^{\text{lan}} = 0.143^{+0.005}_{-0.005}$ for the disk and dynamical components, respectively. The model prefers a somewhat high total binary mass ($2.93 M_\odot$) and mass ratio ($M_1/M_2 = 1.31$) in order to minimize the light-to-heavy and maximize the actinide-to-heavy abundance ratios. The high total mass promotes a prompt collapse, maximizing the neutron richness of the wind ejecta while also minimizing its total ejecta mass. This twofold effect serves to suppress the first *r*-process peak in favor of the heavy *r*-process elements—necessary in the present case of the relatively low first-peak abundances of SPLUS J1424–2542. At the same time, the high neutron star mass ratio promotes a high dynamical ejecta mass, which also serves to lower the light-to-heavy abundance ratio by diluting the wind ejecta with very neutron-rich dynamical ejecta that favor actinide production.

Figure 9 shows the heavy-element abundance pattern of the best-fit neutron star merger model (blue) compared to SPLUS J1424–2542 (red) and the scaled solar *r*-process abundance pattern (yellow). The analytic model is not without its own uncertainties; also shown in Figure 9 are the chemical abundance patterns of 100 random realizations of a $1.66\text{--}1.27 M_\odot$ neutron star merger (gray lines). These uncertainties reflect those of the analytic forms of the ejecta masses described in Dietrich et al. (2020) and Krüger & Foucart (2020; see Holmbeck et al. 2022 for details). Even though there are still some discrepancies between the theoretical predictions and observations (most notably for Sr, La, Tm, and Yb), this model can successfully reproduce the heavy-element abundance pattern of SPLUS J1424–2542. Additional measurements from higher-S/N spectra will help further constrain and refine the models.

4.4. Age and Initial Mass

In Almeida-Fernandes et al. (2023), the chemo-dynamical properties and ages of the 522 metal-poor candidates selected by Placco et al. (2022), which includes SPLUS J1424–2542, were analyzed. Below we discuss the parameters obtained for this particular star and the results are summarized in Table 1.

The age and initial mass of SPLUS J1424–2542 were estimated through a Bayesian isochronal method using MESA Isochrones & Stellar Tracks (MIST; Dotter 2016). Details of the process can be found in Almeida-Fernandes et al. (2023). In Figure 10 we present the cumulative distribution function (CDF) for the age (left panel) and initial mass (right panel) for SPLUS J1424–2542. These parameters were estimated from the median of the distributions (black dashed lines), and the lower and upper limits as the 16th and 84th percentiles (red and blue dashed lines, respectively). For comparison, we also show the distribution of median ages and initial masses for all 522 stars in the Placco et al. (2022) sample as black ticks in the bottom panels, as well as the distributions of the 16th and 84th percentiles as red and blue ticks, respectively.

The CDF in the left panel of Figure 10 shows that the estimated age for SPLUS J1424–2542 is poorly constrained beyond 6 Gyr, i.e., the linear CDF corresponds to a very flat probability distribution at these ages. This CDF results in a very high age uncertainty, where the lower and upper limits differ from the median by about 3 Gyr. Nevertheless, the characterized median age of 10.09 Gyr places SPLUS J1424–2542 among the top 18% oldest stars in the Placco et al. (2022) sample. The CDF in the right panel shows that the initial mass of SPLUS J1424–2542 can be much better constrained. The observed subsolar mass of $0.843^{+0.079}_{-0.056}$ is consistent with the expectation for such an old and metal-poor star.

4.5. Kinematical Parameters

We used the photogeometric distances provided by Bailer-Jones et al. (2021), and the proper motions and line-of-sight velocities of Gaia DR3 (Gaia Collaboration et al. 2023) to calculate the kinematical parameters of SPLUS J1424–2542. Its heliocentric Galactic rectangular velocity vector corresponds to $(U, V, W) = (-93, -29.4, +46.4) \text{ km s}^{-1}$, resulting in a total velocity of $V_{\text{Tot}} = 108.0 \text{ km s}^{-1}$. In Cartesian Galactocentric coordinates, its current position corresponds to $(X, Y, Z) = (2.61, -3.50, 4.22) \text{ kpc}$. Given its current position and total velocity, one can infer that SPLUS J1424–2542 belongs to the Galactic halo.

4.6. Galactic Orbit and Halo Substructure Membership

The orbit of SPLUS J1424–2542 was integrated in a McMillan (2017) Galactic potential using the `galpy` package (Bovy 2015). We adopted a galactocentric distance of $R_{\odot} = 8.21 \text{ kpc}$, with a corresponding rotation velocity of $V_{\odot} = 233.1 \text{ km s}^{-1}$ (McMillan 2017), and a solar velocity of $(U_{\odot}, V_{\odot}, W_{\odot}) = (11.1, 12.24, 7.25) \text{ km s}^{-1}$ (Schönrich et al. 2010). We estimated its orbital parameters, such as apogalactic and perigalactic radius ($R_{\text{apo}}, R_{\text{peri}}$), maximum distance from the Galactic plane (z_{max}), and orbital eccentricity (ecc). We also calculate its angular momentum, energy, and action angles, which allow us to investigate if SPLUS J1424–2542 belongs to any known halo substructure.

In Figure 11 we compare the dynamical properties (top: L_z versus E ; bottom: ecc versus z_{max}) of SPLUS J1424–2542 (yellow star-shaped symbol) with the parameters expected for different galactic substructures, as well as 67 dynamically tagged groups (DTGs). The uncertainties for SPLUS J1424–2542 were computed from the standard deviation of the results from 5000 orbital integrations produced using Monte

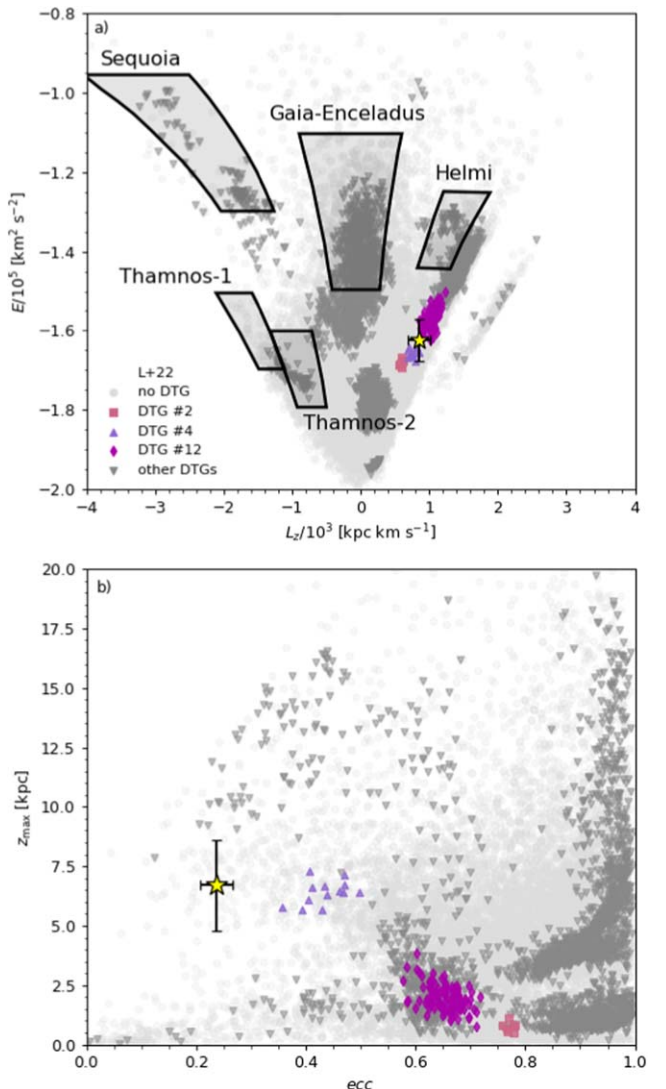


Figure 11. Top panel: comparison between the vertical component of the angular momentum and orbital energy of SPLUS J1424–2542 (yellow star-shaped symbol) to those of known halo substructures (as defined by Koppelman et al. 2019) and DTGs (identified by Lövdal et al. 2022). Bottom panel: eccentricity and maximum distance from the Galactic plane for SPLUS J1424–2542 and the stars in the Lövdal et al. (2022) sample.

Carlo resampling of the astrometry, distances, and radial velocities, taking into account the errors of each parameter. The shaded regions shown in the top panel correspond to the substructures of Sequoia, Thamnos-1 and Thamnos-2, Gaia-Sausage–Enceladus, and Helmi Stream, as defined by Koppelman et al. (2019). Given the observed differences in the vertical component of the angular momentum and in the energy, we can conclude that SPLUS J1424–2542 does not share the same dynamical properties as any of the known halo major substructures.

We also compare the dynamical properties of SPLUS J1424–2542 to those of 67 DTGs identified by Lövdal et al. (2022) using data from Gaia EDR3 (Gaia Collaboration et al. 2021). In Figure 11 we include the sample of Lövdal et al. (2022; light-gray circles), and identify the stars that were assigned to any of the DTGs (gray inverted triangles). In the top panel, we highlight three DTGs that share similar L_z and E as SPLUS J1424–2542, labeled by Lövdal et al. (2022) as DTGs

2 (pink squares), 4 (violet triangles), and 12 (magenta diamonds). However, as seen in the bottom panel, SPLUS J1424–2542 does not share the same values of ecc and z_{\max} as DTGs 2 and 12. Stars in DTG 4 have the same z_{\max} as SPLUS J1424–2542, but their eccentricities are higher by about 0.2. The differences between the dynamical properties of SPLUS J1424–2542 and those of known halo substructures could be indicative that this star belongs to the in situ halo population.

5. Conclusions and Future Work

In this work, we presented a chemo-dynamical analysis of SPLUS J1424–2542, an r -process-enhanced, actinide-boost star observed with the newly commissioned GHOST spectrograph at the Gemini-South telescope. By comparing the light- and heavy-element abundance patterns with yields from theoretical models, we speculate that the gas cloud from which SPLUS J1424–2542 formed must have been enriched by at least two progenitor populations: the supernova explosion of a metal-free 11.3–13.4 M_{\odot} star and the aftermath of a binary neutron star merger with masses 1.66 M_{\odot} and 1.27 M_{\odot} . The mass ($0.843^{+0.079}_{-0.056} M_{\odot}$) and age ($10.09^{+2.96}_{-3.12}$ Gyr) of SPLUS J1424–2542 are consistent with the proposed formation scenario and its kinematics do not connect it with any known structures in the Milky Way halo. Further identification and spectroscopic follow-up of similar objects will help increase our understanding of the formation and chemical evolution of our Galaxy. In this context, GHOST will be a valuable resource for the astronomical community.

Acknowledgments

The authors would like to thank the anonymous referee for constructive comments and Janice Lee, Bryan Miller, and the Gemini staff for their contributions to the GHOST System Verification (SV). The work of V.M.P., K.C., E.D., J.H., V.K., S.X., R.D., M.G., D.H., P.P., C.Q., R.R., C.S., C.U., Z.H., D.J., K.L., B.M., G.P., S.R., and J.T. is supported by NOIRLab, which is managed by the Association of Universities for Research in Astronomy (AURA) under a cooperative agreement with the National Science Foundation. F.A.-F. acknowledges funding for this work from FAPESP grants 2018/20977-2 and 2021/09468-1. I.U.R. acknowledges support from U.S. National Science Foundation (NSF) grants PHY 14-30152 (Physics Frontier Center/JINA-CEE), AST 1815403/1815767, AST 2205847, and the NASA Astrophysics Data Analysis Program, grant 80NSSC21K0627. K.A.V. thanks the National Sciences and Engineering Research Council of Canada for funding through the Discovery Grants and CREATE programs. M.J. acknowledges partial support from the National Research Foundation (NRF) of Korea grant funded by the Ministry of Science and ICT (NRF-2021R1A2C1008679). E.M. acknowledges funding from FAPEMIG under project number APQ-02493-22 and research productivity grant No. 309829/2022-4 awarded by the CNPq, Brazil. Based on observations obtained at the International Gemini Observatory (Program IDs: GS-2021A-Q-419 and GS-2023A-SV-101), a program of NSF's NOIRLab, which is managed by the Association of Universities for Research in Astronomy (AURA) under a cooperative agreement with the National Science Foundation on behalf of the Gemini Observatory partnership: the National Science Foundation (United States), National Research Council

(Canada), Agencia Nacional de Investigación y Desarrollo (Chile), Ministerio de Ciencia, Tecnología e Innovación (Argentina), Ministério da Ciência, Tecnologia, Inovações e Comunicações (Brazil), and Korea Astronomy and Space Science Institute (Republic of Korea). Data were processed using Data Reduction for Astronomy from Gemini Observatory North and South (DRAGONS). GHOST was built by a collaboration between Australian Astronomical Optics at Macquarie University, National Research Council Herzberg of Canada, and the Australian National University, and funded by the International Gemini partnership. The instrument scientist is Dr. Alan McConnachie at NRC, and the instrument team is also led by Dr. Gordon Robertson (at AAO) and Dr. Michael Ireland (at ANU). The authors would like to acknowledge the contributions of the GHOST instrument build team, the Gemini GHOST instrument team, the full SV team, and the rest of the Gemini operations team that were involved in making the SV observations a success. The S-PLUS project, including the T80-South robotic telescope and the S-PLUS scientific survey, was founded as a partnership between the Fundação de Amparo à Pesquisa do Estado de São Paulo (FAPESP), the Observatório Nacional (ON), the Federal University of Sergipe (UFS), and the Federal University of Santa Catarina (UFSC), with important financial and practical contributions from other collaborating institutes in Brazil, Chile (Universidad de La Serena), and Spain (Centro de Estudios de Física del Cosmos de Aragón, CEFCA). We further acknowledge financial support from the São Paulo Research Foundation (FAPESP), the Brazilian National Research Council (CNPq), the Coordination for the Improvement of Higher Education Personnel (CAPES), the Carlos Chagas Filho Rio de Janeiro State Research Foundation (FAPERJ), and the Brazilian Innovation Agency (FINEP). The members of the S-PLUS collaboration are grateful for the contributions from CTIO staff in helping in the construction, commissioning, and maintenance of the T80-South telescope and camera. We are also indebted to René Laporte, INPE, and Keith Taylor for their important contributions to the project. From CEFCA, we thank Antonio Marín-Franch for invaluable contributions in the early phases of the project, David Cristóbal-Hornillos and the team for their help with the installation of the data reduction package JYPE version 0.9.9, César Íñiguez for providing 2D measurements of the filter transmissions, and all other staff members for their support with various aspects of the project. IRAF was distributed by the National Optical Astronomy Observatory, which was managed by AURA under a cooperative agreement with the NSF. This research has made use of NASA's Astrophysics Data System Bibliographic Services; the arXiv pre-print server operated by Cornell University; the SIMBAD database hosted by the Strasbourg Astronomical Data Center; and the online Q&A platform stackoverflow (<http://stackoverflow.com/>).

Facilities: Gemini:South (GMOS) and Gemini:South (GHOST).

Software: awk (Aho et al. 1987), dustmaps (Green 2018), DRAGONS (Labrie et al. 2019, 2022), gnuplot (Williams & Kelley 2015), IRAF (Tody 1986, 1993), linemake (Placco et al. 2021a, 2021b), MOOG (Sneden 1973), numpy (Harris 2020), pandas (McKinney 2010), sed (McMahon 1983), and stilts (Taylor 2006).

ORCID iDs

- Vinicio M. Placco [DOI](https://orcid.org/0000-0003-4479-1265)
- Felipe Almeida-Fernandes [DOI](https://orcid.org/0000-0002-8048-8717)
- Erika M. Holmbeck [DOI](https://orcid.org/0000-0002-5463-6800)
- Ian U. Roederer [DOI](https://orcid.org/0000-0001-5107-8930)
- Mohammad K. Mardini [DOI](https://orcid.org/0000-0001-9178-3992)
- Christian R. Hayes [DOI](https://orcid.org/0000-0003-2969-2445)
- Kim Venn [DOI](https://orcid.org/0000-0003-4134-2042)
- Kristin Chiboucas [DOI](https://orcid.org/0000-0002-9020-5004)
- Emily Deibert [DOI](https://orcid.org/0000-0001-9796-2158)
- Roberto Gamen [DOI](https://orcid.org/0000-0002-5227-9627)
- Jeong-Eun Heo [DOI](https://orcid.org/0000-0003-2530-3000)
- Miji Jeong [DOI](https://orcid.org/0009-0009-7838-7771)
- Venu Kalari [DOI](https://orcid.org/0000-0002-4641-2532)
- Eder Martioli [DOI](https://orcid.org/0000-0002-5084-168X)
- Siyi Xu [DOI](https://orcid.org/0000-0002-8808-4282)
- Ruben Diaz [DOI](https://orcid.org/0000-0001-9716-5335)
- Carlos Quiroz [DOI](https://orcid.org/0000-0001-5558-6297)
- Roque Ruiz-Carmona [DOI](https://orcid.org/0000-0001-7518-1393)
- Chris Simpson [DOI](https://orcid.org/0000-0001-8589-4055)
- Alan W. McConnachie [DOI](https://orcid.org/0000-0003-4666-6564)
- Michael Ireland [DOI](https://orcid.org/0000-0002-6194-043X)
- Trystyn A. M. Berg [DOI](https://orcid.org/0000-0002-2606-5078)
- J. Gordon Robertson [DOI](https://orcid.org/0000-0001-5528-7801)
- Zachary Hartman [DOI](https://orcid.org/0000-0003-4236-6927)
- David O. Jones [DOI](https://orcid.org/0000-0002-6230-0151)
- Kathleen Labrie [DOI](https://orcid.org/0000-0002-6633-7891)
- Joanna Thomas-Osip [DOI](https://orcid.org/0000-0003-1033-4402)

References

- Abbott, B. P., Abbott, R., Abbott, T. D., et al. 2017, *ApJL*, **848**, L12
- Abholaima, A., & Frebel, A. 2018, *ApJS*, **238**, 36
- Abuchaim, Y., Perrottoni, H. D., Rossi, S., et al. 2023, *ApJ*, **949**, 48
- Aho, A. V., Kernighan, B. W., & Weinberger, P. J. 1987, The AWK Programming Language (Boston, MA: Addison-Wesley Longman Publishing Co., Inc.)
- Almeida-Fernandes, F., Placco, V. M., Rocha-Pinto, H. J., et al. 2023, *MNRAS*, **523**, 2934
- Almeida-Fernandes, F., SamPedro, L., Herpich, F. R., et al. 2022, *MNRAS*, **511**, 4590
- Aoki, W., Honda, S., Beers, T. C., et al. 2007, *ApJ*, **660**, 747
- Asplund, M., Grevesse, N., Sauval, A. J., & Scott, P. 2009, *ARA&A*, **47**, 481
- Bailer-Jones, C. A. L., Rybizki, J., Fouesneau, M., Demleitner, M., & Andrae, R. 2021, *AJ*, **161**, 147
- Barklem, P. S., Christlieb, N., Beers, T. C., et al. 2005, *A&A*, **439**, 129
- Baxandall, F. E. 1913, *MNRAS*, **74**, 32
- Bovy, J. 2015, *ApJS*, **216**, 29
- Burbidge, E. M., Burbidge, G. R., Fowler, W. A., & Hoyle, F. 1957, *RvMP*, **29**, 547
- Burris, D. L., Pilachowski, C. A., Armandroff, T. E., et al. 2000, *ApJ*, **544**, 302
- Cain, M., Frebel, A., Gull, M., et al. 2018, *ApJ*, **864**, 43
- Cain, M., Frebel, A., Ji, A. P., et al. 2020, *ApJ*, **898**, 40
- Casagrande, L., & Vandenberg, D. A. 2014, *MNRAS*, **444**, 392
- Castelli, F., & Kurucz, R. L. 2003, in IAU Symp., 210, Modelling of Stellar Atmospheres, ed. N. Piskunov (Cambridge: Cambridge Univ. Press), A20
- Christlieb, N., Beers, T. C., Barklem, P. S., et al. 2004b, *A&A*, **428**, 1027
- Christlieb, N., Gustafsson, B., Korn, A. J., et al. 2004a, *ApJ*, **603**, 708
- Cohen, J. G., Christlieb, N., Qian, Y. Z., & Wasserburg, G. J. 2003, *ApJ*, **588**, 1082
- Cowan, J. J., Sneden, C., Burles, S., et al. 2002, *ApJ*, **572**, 861
- Cowley, C. R., Hartoog, M. R., Aller, M. F., & Cowley, A. P. 1973, *ApJ*, **183**, 127
- Cui, W. Y., Sivarani, T., & Christlieb, N. 2013, *A&A*, **558**, A36
- Da Costa, G. S., Bessell, M. S., Mackey, A. D., et al. 2019, *MNRAS*, **489**, 5900
- Davies, R. L., Allington-Smith, J. R., Bettess, P., et al. 1997, *Proc. SPIE*, **2871**, 1099
- Dietrich, T., Coughlin, M. W., Pang, P. T. H., et al. 2020, *Sci*, **370**, 1450
- Dotter, A. 2016, *ApJS*, **222**, 8
- Drout, M. R., Piro, A. L., Shappee, B. J., et al. 2017, *Sci*, **358**, 1570
- Dyson, F. W. 1906, *RSPTA*, **206**, 403
- Ezzeddine, R., Rasmussen, K., Frebel, A., et al. 2020, *ApJ*, **898**, 150
- Frebel, A. 2018, *ARNPS*, **68**, 237
- Frebel, A., Chiti, A., Ji, A. P., Jacobson, H. R., & Placco, V. M. 2015, *ApJL*, **810**, L27
- Frebel, A., Christlieb, N., Norris, J. E., et al. 2006, *ApJ*, **652**, 1585
- Frebel, A., Christlieb, N., Norris, J. E., et al. 2007, *ApJL*, **660**, L117
- Gaia Collaboration, Brown, A. G. A., Vallenari, A., et al. 2021, *A&A*, **649**, A1
- Gaia Collaboration, Vallenari, A., Brown, A. G. A., et al. 2023, *A&A*, **674**, A1
- Gilroy, K. K., Sneden, C., Pilachowski, C. A., & Cowan, J. J. 1988, *ApJ*, **327**, 298
- Gimeno, G., Roth, K., Chiboucas, K., et al. 2016, *Proc. SPIE*, **9908**, 99082S
- Goriely, S., Bauswein, A., & Janka, H.-T. 2011, *ApJL*, **738**, L32
- Green, G. 2018, *JOSS*, **3**, 695
- Grichener, A., & Soeker, N. 2019, *ApJ*, **878**, 24
- Gudin, D., Shank, D., Beers, T. C., et al. 2021, *ApJ*, **908**, 79
- Gull, M., Frebel, A., Cain, M. G., et al. 2018, *ApJ*, **862**, 174
- Hansen, T. T., Holmbeck, E. M., Beers, T. C., et al. 2018, *ApJ*, **858**, 92
- Hansen, T. T., Simon, J. D., Marshall, J. L., et al. 2017, *ApJ*, **838**, 44
- Harris, C. R., Millman, K. J., van der Walt, S. J., et al. 2020, *Natur*, **585**, 357
- Hartwig, T., Yoshida, N., Magg, M., et al. 2018, *MNRAS*, **478**, 1795
- Hayek, W., Wiesendahl, U., Christlieb, N., et al. 2009, *A&A*, **504**, 511
- Hayes, C. R., Venn, K. A., Waller, F., et al. 2023, *ApJ*, **955**, 17
- Hayes, C. R., Waller, F., Ireland, M., et al. 2022, *Proc. SPIE*, **12184**, 121846H
- Heger, A., & Woosley, S. E. 2010, *ApJ*, **724**, 341
- Hill, V., Christlieb, N., Beers, T. C., et al. 2017, *A&A*, **607**, A91
- Holmbeck, E., Hansen, T. T., Beers, T. C., et al. 2020, *ApJS*, **249**, 30
- Holmbeck, E. M., Beers, T. C., Roederer, I. U., et al. 2018, *ApJL*, **859**, L24
- Holmbeck, E. M., Frebel, A., McLaughlin, G. C., et al. 2021, *ApJ*, **909**, 21
- Holmbeck, E. M., O'Shaughnessy, R., Delfavero, V., & Belczynski, K. 2022, *ApJ*, **926**, 196
- Holmbeck, E. M., Sprouse, T. M., Mumpower, M. R., et al. 2019, *ApJ*, **870**, 23
- Honda, S., Aoki, W., Kajino, T., et al. 2004, *ApJ*, **607**, 474
- Hoyle, F. 1946, *MNRAS*, **106**, 343
- Ireland, M., Anthony, A., Burley, G., et al. 2014, *Proc. SPIE*, **9147**, 91471J
- Ireland, M. J., White, M., Bento, J. P., et al. 2018, *Proc. SPIE*, **10707**, 070735
- Ivans, I. I., Simmerer, J., Sneden, C., et al. 2006, *ApJ*, **645**, 613
- Ji, A. P., & Frebel, A. 2018, *ApJ*, **856**, 138
- Ji, A. P., Frebel, A., Chiti, A., & Simon, J. D. 2016, *Natur*, **531**, 610
- Jonsell, K., Barklem, P. S., Gustafsson, B., et al. 2006, *A&A*, **451**, 651
- Koppelman, H. H., Helmi, A., Massari, D., Price-Whelan, A. M., & Starkenburg, T. K. 2019, *A&A*, **631**, L9
- Krüger, C. J., & Foucart, F. 2020, *PhRvD*, **101**, 103002
- Labrie, K., Anderson, K., Cárdenes, R., Simpson, C., & Turner, J. E. H. 2019, in ASP Conf. Ser. 523, Astronomical Data Analysis Software and Systems XXVII, ed. P. J. Teuben et al. (San Francisco, CA: ASP), 321
- Labrie, K., Simpson, C., Anderson, K., et al. 2022, DRAGONS, v3.0.4, Zenodo, doi:10.5281/zenodo.7308726
- Lindegren, L., Bastian, U., Biermann, M., et al. 2021, *A&A*, **649**, A4
- Lövdal, S. S., Ruiz-Lara, T., Koppelman, H. H., et al. 2022, *A&A*, **665**, A57
- Luck, R. E., & Bond, H. E. 1981, *ApJ*, **244**, 919
- Lunt, J. 1907, *RSPSA*, **79**, 118
- Mardini, M. K., Placco, V. M., Meiron, Y., et al. 2020, *ApJ*, **903**, 88
- Mashonkina, L., & Christlieb, N. 2014, *A&A*, **565**, A123
- Mashonkina, L., Christlieb, N., Barklem, P. S., et al. 2010a, *A&A*, **516**, A46
- Mashonkina, L., Christlieb, N., Barklem, P. S., et al. 2010b, *A&A*, **516**, A46
- Mashonkina, L., Christlieb, N., Barklem, P. S., et al. 2014a, *A&A*, **569**, A43
- Mashonkina, L., Christlieb, N., Barklem, P. S., et al. 2014b, *A&A*, **569**, A43
- McConnachie, A. W., Hayes, C. R., Pazder, J., et al. 2022, *NatAs*, **6**, 1491
- McKinney, W. 2010, in Proc. of the 9th Python in Science Conf. 51, ed. S. van der Walt & J. Millman (Austin, TX: SciPy), 56
- Mcmahon, L. E. 1983, UNIX Programmer's Manual, 2 (7th ed.; Murray Hill, NJ: Bell Telephone Laboratories, Incorporated), 440
- McMillan, P. J. 2017, *MNRAS*, **465**, 76
- Mendes de Oliveira, C., Ribeiro, T., Schoenell, W., et al. 2019, *MNRAS*, **489**, 241

- Merrill, P. W. 1926, *ApJ*, **63**, 13
- Mucciarelli, A., Bellazzini, M., & Massari, D. 2021, *A&A*, **653**, A90
- Nordlander, T., & Lind, K. 2017, *A&A*, **607**, A75
- Placco, V. M., Almeida-Fernandes, F., Arentsen, A., et al. 2022, *ApJS*, **262**, 8
- Placco, V. M., Beers, T. C., Ivans, I. I., et al. 2015b, *ApJ*, **812**, 109
- Placco, V. M., Beers, T. C., Santucci, R. M., et al. 2018, *AJ*, **155**, 256
- Placco, V. M., Frebel, A., Beers, T. C., et al. 2013, *ApJ*, **770**, 104
- Placco, V. M., Frebel, A., Beers, T. C., et al. 2016, *ApJ*, **833**, 21
- Placco, V. M., Frebel, A., Beers, T. C., & Stancliffe, R. J. 2014, *ApJ*, **797**, 21
- Placco, V. M., Frebel, A., Lee, Y. S., et al. 2015a, *ApJ*, **809**, 136
- Placco, V. M., Holmbeck, E. M., Frebel, A., et al. 2017, *ApJ*, **844**, 18
- Placco, V. M., Roederer, I. U., Lee, Y. S., et al. 2021c, *ApJL*, **912**, L32
- Placco, V. M., Santucci, R. M., Beers, T. C., et al. 2019, *ApJ*, **870**, 122
- Placco, V. M., Santucci, R. M., Yuan, Z., et al. 2020, *ApJ*, **897**, 78
- Placco, V. M., Sneden, C., Roederer, I. U., et al. 2021a, *RNAAS*, **5**, 92
- Placco, V. M., Sneden, C., Roederer, I. U., et al., 2021b linemake: Line list generator v1.0, Astrophysics Source Code Library, ascl:[2104.027](https://ascl.net/2104.027)
- Ren, J., Christlieb, N., & Zhao, G. 2012, *A&A*, **537**, A118
- Roederer, I. U., Cowan, J. J., Karakas, A. I., et al. 2010, *ApJ*, **724**, 975
- Roederer, I. U., Hattori, K., & Valluri, M. 2018a, *AJ*, **156**, 179
- Roederer, I. U., Lawler, J. E., Den Hartog, E. A., et al. 2022, *ApJS*, **260**, 27
- Roederer, I. U., Lawler, J. E., Sneden, C., et al. 2008, *ApJ*, **675**, 723
- Roederer, I. U., Lawler, J. E., Sobeck, J. S., et al. 2012, *ApJS*, **203**, 27
- Roederer, I. U., Placco, V. M., & Beers, T. C. 2016, *ApJL*, **824**, L19
- Roederer, I. U., Preston, G. W., Thompson, I. B., et al. 2014, *AJ*, **147**, 136
- Roederer, I. U., Sakari, C. M., Placco, V. M., et al. 2018b, *ApJ*, **865**, 129
- Sakari, C. M., Placco, V. M., Farrell, E. M., et al. 2018b, *ApJ*, **868**, 110
- Sakari, C. M., Placco, V. M., Hansen, T., et al. 2018a, *ApJL*, **854**, L20
- Sakari, C. M., Roederer, I. U., Placco, V. M., et al. 2019, *ApJ*, **874**, 148
- Skúladóttir, Á., Salvadori, S., Amarsi, A. M., et al. 2021, *ApJL*, **915**, L30
- Schlafly, E. F., & Finkbeiner, D. P. 2011, *ApJ*, **737**, 103
- Schönrich, R., Binney, J., & Dehnen, W. 2010, *MNRAS*, **403**, 1829
- Shank, D., Beers, T. C., Placco, V. M., et al. 2023, *ApJ*, **943**, 23
- Shappee, B. J., Simon, J. D., Drout, M. R., et al. 2017, *Sci*, **358**, 1574
- Siegel, D. M., Barnes, J., & Metzger, B. D. 2019, *Natur*, **569**, 241
- Siqueira Mello, C., Hill, V., Barbuy, B., et al. 2014, *A&A*, **565**, A93
- Skrutskie, M. F., Cutri, R. M., Stiening, R., et al. 2006, *AJ*, **131**, 1163
- Sneden, C., Cowan, J. J., & Gallino, R. 2008, *ARA&A*, **46**, 241
- Sneden, C., Cowan, J. J., Lawler, J. E., et al. 2003, *ApJ*, **591**, 936
- Sneden, C., & Pilachowski, C. A. 1985, *ApJL*, **288**, L55
- Sneden, C., Preston, G. W., McWilliam, A., & Searle, L. 1994, *ApJL*, **431**, L27
- Sneden, C. A. 1973, PhD thesis, The University of Texas at Austin
- Spite, M., & Spite, F. 1978, *A&A*, **67**, 23
- Taylor, M. B. 2006, in ASP Conf. Ser. 351, Astronomical Data Analysis Software and Systems XV, ed. C. Gabriel et al. (San Francisco, CA: ASP), **666**
- Tody, D. 1986, *Proc. SPIE*, **627**, 733
- Tody, D. 1993, in ASP Conf. Ser. 52, Astronomical Data Analysis Software and Systems II, ed. R. J. Hanisch, R. J. V. Brissenden, & J. Barnes (San Francisco, CA: ASP), **173**
- Truran, J. W. 1981, *A&A*, **97**, 391
- Vincenzo, F., Matteucci, F., Recchi, S., et al. 2015, *MNRAS*, **449**, 1327
- Westin, J., Sneden, C., Gustafsson, B., & Cowan, J. J. 2000, *ApJ*, **530**, 783
- Williams, T., & Kelley, C. 2015, Gnuplot 5.0: an interactive plotting program, <http://www.gnuplot.info/>
- Wolf, C., Onken, C. A., Luvaal, L. C., et al. 2018, *PASA*, **35**, e010
- Xing, Q.-F., Zhao, G., Aoki, W., et al. 2019, *NatAs*, **3**, 631
- Yuan, Z., Myeong, G. C., Beers, T. C., et al. 2020, *ApJ*, **891**, 39